Reduced Quadrature for Finite Element and Isogeometric Methods in Nonlinear Solids

Weican Li[a], Georgios Moutsanidis[b,c], Masoud Behzadinasab[a], Michael Hillman[d], Yuri Bazilevs[a]

[a]*School of Engineering, Brown University, 184 Hope St., Providence, RI 02912, USA*
[b]*Department of Civil Engineering, Stony Brook University, Stony Brook, NY 11794, USA*
[c]*Institute for Advanced Computational Science, Stony Brook, NY 11794, USA*
[d]*Department of Civil and Environmental Engineering,*
The Pennsylvania State University, University Park, PA 16802, USA

Abstract

We extend the recently proposed framework using reduced quadrature in the Finite Element and Isogeometric methods for solid mechanics to the nonlinear realm. The proposed approach makes use of the governing equations in the updated Lagrangian formulation in combination with the rate form of the constitutive laws. The key ingredient in the framework is the careful development and use of the Taylor series expansion in the integrands of the internal work terms. The resulting formulation relies on the evaluation of stress gradients, for which the evolution equations and update algorithms are developed. The versatility of the proposed approach is demonstrated on an extensive set of numerical examples employing a variety of constitutive models. The resulting formulations are especially effective in alleviating volumetric locking for the cases of nearly-incompressible and plastic deformations.

Keywords: One-point quadrature, Volumetric locking, Isogeometric Analysis (IGA), Taylor series expansion, Plasticity, M7 Microplane model

1. Introduction

In [1] the authors developed a new approach to numerical quadrature in computational solids that is based on the idea of Taylor expansion of the integrated quantities, focusing on the treatment of the stress terms. This was done in an effort to: 1. Reduce the computational costs associated with the traditional Gaussian quadrature; 2. Develop a parameter-free framework for stabilizing reduced-integration approaches; and 3. Provide accurate and stable methods for the discretizations that rely on the nodal quadrature, such as meshfree methods [2]. Although the formulation in [1] assumed linear elasticity and rectangular element topology, applications to FEM (linear and quadratic), NURBS-based IGA [3, 4], and the Material-Point Method (MPM) [5] using IGA as

---

the discretization [6] were presented to illustrate the method's broader applicability. An important development in [1] was the treatment of near-incompressibility where the corrections coming from the Taylor series expansion were only applied to the deviatoric part of the stress. This construction alleviated volumetric locking issues without the need to introduce suitable auxiliary pressure approximation spaces, a significant benefit for the discretizations of higher order and continuity. Another important finding in [1] was the need to use the Taylor series expansion up to second order to fully eliminate zero-energy modes from 3D linear hexahedral discretizations.

In the present work, we extent the ideas and methods developed in [1] to the nonlinear realm. Before proceeding, we note that the use of the Taylor series expansion in the evaluation of internal work terms in the FEM and related methods is not new. The first papers appeared in the early-to-mid 80s [7, 8] and were aimed at addressing the instability of one-point quadrature methods and improving the performance of hourglass control techniques [9, 10]. After a fairly long pause, in [11], the authors used the Taylor expansion of the first PK stress in the framework of the total Lagrangian formulation, and combined it with the more traditional artificial stiffness technique (still requiring a tunable parameter) to develop nonlinear large-deformation solid formulations. The work in [11] was recently extended to include a gradient-extended damage model. Nodal integration in meshfree methods, such as the Reproducing Kernel Particle Method (RKPM) [12, 13], suffers very similar issues as one-point quadrature in FEM. Because of the smoothness of meshfree approximations, short wavelength modes with zero gradient at nodal locations can be admitted in the solution with little to no resistance, which often leads to severe node-to-node oscillations in the numerical results [14–16]. Stress points [17–19] and sub-domain type methods [20–23] have also been utilized to avoid the instability, but this is akin to expensive high-order quadrature. The Taylor series expansion approach of [7] has been employed for meshfree methods in [24, 25] and later developed with implicit gradients in [26, 27] to provide a low-cost, practical solution [28]. Nevertheless, the nonlinear formulations need approximate material tangents [28]. Overall, the sub-domain methods, least-squares methods [15, 29, 30], and Taylor series methods all necessitate stress-gradient type terms whose development is lacking and is also address in the present paper.

Methods of reduced quadrature for IGA are often based on finding an optimal set of points (or a near-optimal set, like the Greville points) and weights that can exactly integrate piece-wise polynomial functions with a given degree of continuity [31, 32]. More recently, reduced Gauss quadrature rules, as well as a combination of Gauss-point- and Greville-point-based rules were developed in [33, 34] for IGA. These approaches significantly reduced the number of quadrature points required for IGA relative to the full Gauss quadrature because the continuity of B-Spline functions was explicitly taken into account when constructing these rules. However, these rules are quite specialized to NURBS-based IGA in that they rely on the knot-vector or patch structure of the NURBS meshes. In addition, near-incompressibility, which is important in many applications,

is not explicitly addressed by these methods.

In the present work, we're guided by the considerations of: 1. Relative method simplicity; 2. Circumvention of tunable parameters; 3. Direct applicability to a large class of discretizations (FEM, IGA, meshfree methods) and constitutive models; and 4. Proper treatment of large deformations. For this, our proposed formulation includes the following items and features. We work with the governing equations in the updated Lagrangian form [35] and assume that the constitutive laws are written in the rate form. In the internal work terms, both the Cauchy stress and strain-displacement (or strain-rate-velocity) matrix are expanded in the Taylor series up to second order in the element parametric variable. The Taylor expansion results in the structure of the internal work integral that includes the one-point quadrature term and correction terms that depend on the first and second parametric gradients of the Cauchy stress. Given a choice of the objective rate of stress, time-evolution equations and update algorithms are developed for the stress and its parametric gradients. The stress gradient updates make use of the material tangent stiffness matrix, which, if not available in the analytical form, may be approximated using a finite-difference approach. (The original idea to introduce the rate form of the stress gradient equation and develop its update is from [36].) Ideas from the B-bar formulation [37, 38] are used to develop the correction terms such that volumetric locking is avoided for the cases of nearly-incompressible and plastic deformations.

The paper is organized as follows. In Section 2 we develop the core constituents of the proposed framework, including the evolution equations and update algorithms for the stress parametric gradients, linearization of the resulting correction terms, treatment of near-incompressibility, and reduction to the 2D case. In Section 3 we show how our proposed framework applies to several popular constitutive models, namely, hyperelasticity, Von Mises plasticity, and the M7 Microplane model of concrete failure [39]. In Section 4 we show several numerical examples using both linear FEM and quadratic NURBS discretizations. In Section 5 we draw conclusions.

2. Theoretical Framework

2.1. Core Formulation

We start from the weak form of the updated Lagrangian formulation of solid mechanics: Find $\mathbf{v}$, such that for all $\mathbf{w}$

$$\int_\Omega \mathbf{w} \cdot \rho \frac{\partial \mathbf{v}}{\partial t}\bigg|_X d\Omega + \int_\Omega \nabla \mathbf{w} : \boldsymbol{\sigma} \, d\Omega - \int_\Omega \mathbf{w} \cdot \rho \mathbf{f} \, d\Omega - \int_{\Gamma_h} \mathbf{w} \cdot \mathbf{h} \, d\Gamma = 0, \tag{1}$$

where $\mathbf{v}$ is the velocity vector, $\frac{\partial \mathbf{v}}{\partial t}\big|_X$ is the acceleration vector, $\mathbf{w}$ is the vector-valued test function, Ω is the solid-object current configuration, $\boldsymbol{\sigma}$ is the Cauchy stress, ρ is the solid density in the current

configuration, $\mathbf{f}$ is the body force per unit mass, and $\mathbf{h}$ is the applied traction on the boundary Γ_h.

Let $d = 2, 3$ denote the number of space dimensions. The Galerkin approximation of the above weak form leads to the following set of discrete nonlinear equations:

$$R_{Ai} = \int_\Omega N_A \rho \frac{\partial v_i^h}{\partial t}\Big|_X \, d\Omega + \int_\Omega B_{AIi} \sigma_I \, d\Omega - \int_\Omega N_A \rho f_i \, d\Omega - \int_{\Gamma_h} N_A h_i \, d\Gamma = 0, \qquad (2)$$

where A is the nodal or control-point index, $i = 1, \ldots, d$ is the Cartesian-direction index, $I = 1, \ldots, d(d+1)/2$ is the Voigt-notation index, N_A is the Ath basis function, and B_{AIj}'s are the components of the strain-displacement or strain rate-velocity matrix given by

$$\mathbf{B}_A = \begin{bmatrix} N_{A,x_1} & 0 \\ 0 & N_{A,x_2} \\ N_{A,x_2} & N_{A,x_1} \end{bmatrix} \qquad (3)$$

in 2D and

$$\mathbf{B}_A = \begin{bmatrix} N_{A,x_1} & 0 & 0 \\ 0 & N_{A,x_2} & 0 \\ 0 & 0 & N_{A,x_3} \\ 0 & N_{A,x_3} & N_{A,x_2} \\ N_{A,x_3} & 0 & N_{A,x_1} \\ N_{A,x_2} & N_{A,x_1} & 0 \end{bmatrix} \qquad (4)$$

in 3D. Here and in what follows, comma denotes partial differentiation. The remaining developments assume 3D unless specified otherwise. Note that in the updated Lagrangian formulation employed in this work the partial derivatives are taken with respect to the spatial coordinates of the current configuration.

Following the developments in [1], we expand the internal work in Taylor series to second order as follows:

$$\int_{\Omega_e} \mathbf{B}_A^T \boldsymbol{\sigma} \, d\Omega = \int_\square \mathbf{B}_A^T \boldsymbol{\sigma} J_\xi \, d\square \approx J_\xi(\mathbf{0}) \int_\square \left(\mathbf{B}_A^T(\mathbf{0}) + \xi_i \mathbf{B}_{A,\xi_i}^T(\mathbf{0}) + \frac{1}{2} \xi_k \xi_l \mathbf{B}_{A,\xi_k \xi_l}^T(\mathbf{0}) \right)$$
$$\left(\boldsymbol{\sigma}(\mathbf{0}) + \xi_j \boldsymbol{\sigma}_{,\xi_j}(\mathbf{0}) + \frac{1}{2} \xi_m \xi_n \boldsymbol{\sigma}_{,\xi_m \xi_n}(\mathbf{0}) \right) d\square. \qquad (5)$$

Here, Ω_e is the integration zone (e.g., a finite element) in the current configuration mapped from a parametric domain denoted by $\square$, $\boldsymbol{\xi}$ are the parametric coordinates, and J_ξ is the Jacobian determinant of the mapping between the parametric and physical domains. The latter quantity is assumed to vary little over the integration-zone domain and is approximated by its value at the element midpoint. The present work assumes that the parametric domain is a bi-unit square in 2D or a bi-unit

cube in 3D.

In Equation (5), most cross-terms involving odd-order polynomial modes integrate to zero in the parametric domain. Ignoring the remaining cross-terms we simplify Equation (5) as

$$\int_{\Omega_e} \mathbf{B}_A^T \boldsymbol{\sigma} \, d\Omega \approx \left(J_{\xi}(\mathbf{0}) \int_{\square} d\square \right) \mathbf{B}_A^T(\mathbf{0})\boldsymbol{\sigma}(\mathbf{0}) + \left(J_{\xi}(\mathbf{0}) \int_{\square} \xi_i \xi_j \, d\square \right) \mathbf{B}_{A,\xi_i}^T(\mathbf{0})\boldsymbol{\sigma}_{,\xi_j}(\mathbf{0})$$
$$+ \left(\frac{J_{\xi}(\mathbf{0})}{4} \int_{\square} \xi_k \xi_l \xi_m \xi_n \, d\square \right) \mathbf{B}_{A,\xi_k\xi_l}^T(\mathbf{0})\boldsymbol{\sigma}_{,\xi_m\xi_n}(\mathbf{0}). \tag{6}$$

Note that the integrals in the parentheses may be computed analytically with the values provided in [1] for both the 2D and 3D cases. Furthermore, the moment matrix $\int_{\square} \xi_i \xi_j \, d\square$ may be expressed as a constant times the identity matrix for a bi-unit square or cube parametric domains.

The first term on the right hand side of Equation (6) corresponds to the traditional one-point Gaussian quadrature technique, while the second and third terms represent the first-and second-order corrections [1], respectively, and require the values of the *parametric derivatives* of the $\mathbf{B}_A$ matrix as well as the Cauchy stress. The former object may be expressed in 3D as follows:

$$\mathbf{B}_{A,\xi_i} = \begin{bmatrix} N_{A,x_1\xi_i} & 0 & 0 \\ 0 & N_{A,x_2\xi_i} & 0 \\ 0 & 0 & N_{A,x_3\xi_i} \\ 0 & N_{A,x_3\xi_i} & N_{A,x_2\xi_i} \\ N_{A,x_3\xi_i} & 0 & N_{A,x_1\xi_i} \\ N_{A,x_2\xi_i} & N_{A,x_1\xi_i} & 0 \end{bmatrix} , \ \mathbf{B}_{A,\xi_i\xi_j} = \begin{bmatrix} N_{A,x_1\xi_i\xi_j} & 0 & 0 \\ 0 & N_{A,x_2\xi_i\xi_j} & 0 \\ 0 & 0 & N_{A,x_3\xi_i\xi_j} \\ 0 & N_{A,x_3\xi_i\xi_j} & N_{A,x_2\xi_i\xi_j} \\ N_{A,x_3\xi_i\xi_j} & 0 & N_{A,x_1\xi_i\xi_j} \\ N_{A,x_2\xi_i\xi_j} & N_{A,x_1\xi_i\xi_j} & 0 \end{bmatrix}, \tag{7}$$

with the mixed basis-function derivatives are approximated as

$$N_{A,x_k\xi_i} \approx N_{A,\xi_l\xi_i} \, [\mathbf{x}_{\boldsymbol{\xi}}^{-1}(\mathbf{0})]_{lk} \, , \ N_{A,x_k\xi_i\xi_j} \approx N_{A,\xi_l\xi_i\xi_j} \, [\mathbf{x}_{\boldsymbol{\xi}}^{-1}(\mathbf{0})]_{lk}. \tag{8}$$

Here, as before, the Jacobian of the transformation between the physical and parametric domains $\mathbf{x}_{\boldsymbol{\xi}}$ is assumed to show little variation over the integration domain and is approximated by its value at the midpoint of the parametric domain.

2.2. Evolution of the Cauchy Stress and Its Gradients

To develop the expressions for the Cauchy stress and its parametric derivatives that are applicable to a large class of material models we will work with a rate form of the constitutive equations. We adopt the Truesdell rate of the Cauchy stress $\dot{\boldsymbol{\sigma}}^{\mathrm{Tr}}$, which may be expressed as [40]:

$$\dot{\boldsymbol{\sigma}}^{\mathrm{Tr}} = \dot{\boldsymbol{\sigma}} + (\nabla \cdot \mathbf{v}) \, \boldsymbol{\sigma} - \nabla \mathbf{v} \, \boldsymbol{\sigma} - \boldsymbol{\sigma} \, \nabla \mathbf{v}^T, \tag{9}$$

5

where $\dot{\boldsymbol{\sigma}}$ is the material time derivative of the Cauchy stress. We also assume a constitutive law of the form

$$\dot{\boldsymbol{\sigma}}^{\text{Tr}} = \mathcal{H}(\boldsymbol{\sigma}, \nabla \mathbf{v}) \tag{10}$$

where $\mathcal{H}$ is a response function. We will consider special cases of $\mathcal{H}$ in the later parts of the paper. Combining Equations (9) and (10) and rearranging terms gives a time-continuous evolution equation for the Cauchy stress

$$\dot{\boldsymbol{\sigma}} = \mathcal{H}(\boldsymbol{\sigma}, \nabla \mathbf{v}) - (\nabla \cdot \mathbf{v}) \, \boldsymbol{\sigma} + \nabla \mathbf{v} \, \boldsymbol{\sigma} + \boldsymbol{\sigma} \, \nabla \mathbf{v}^T \tag{11}$$

Integrating this equation in time at the midpoint of each integration zone gives the Cauchy stress needed to evaluate the first term on the right hand side of Equation (6).

In order to evaluate the second term on the right hand side of Equation (6), following the ideas from [36], we differentiate both sides of Equation (11) with respect to the parametric coordinates $\boldsymbol{\xi}$ to obtain

$$(\dot{\boldsymbol{\sigma}}_{,\xi_i}) = \mathcal{H}_{,\xi_i}(\boldsymbol{\sigma}, \nabla \mathbf{v}) - (\nabla \cdot \mathbf{v})_{,\xi_i} \, \boldsymbol{\sigma} - (\nabla \cdot \mathbf{v}) \, \boldsymbol{\sigma}_{,\xi_i} + \nabla \mathbf{v}_{,\xi_i} \, \boldsymbol{\sigma} + \nabla \mathbf{v} \, \boldsymbol{\sigma}_{,\xi_i} + \boldsymbol{\sigma}_{,\xi_i} \, \nabla \mathbf{v}^T + \boldsymbol{\sigma} \, \nabla \mathbf{v}^T_{,\xi_i}. \tag{12}$$

Equation (12) now defines the evolution equation for the Cauchy stress parametric gradient. Integrating this equation in time at the midpoint of each integration zone produces the Cauchy stress parametric gradient needed to evaluate the second term on the right hand side of Equation (6). Note that because the partial derivatives are taken with respect to the time-independent parametric coordinates, we are able to interchange the order of space and time differentiation on the left side of Equation (12). Similarly, differentiating both sides of Equation (12) with respect to $\boldsymbol{\xi}$ results in

$$\begin{aligned} (\dot{\boldsymbol{\sigma}}_{,\xi_i\xi_j}) = {} & \mathcal{H}_{,\xi_i\xi_j}(\boldsymbol{\sigma}, \nabla \mathbf{v}) - (\nabla \cdot \mathbf{v})_{,\xi_i\xi_j} \, \boldsymbol{\sigma} - (\nabla \cdot \mathbf{v})_{,\xi_i} \, \boldsymbol{\sigma}_{,\xi_j} - (\nabla \cdot \mathbf{v}) \, \boldsymbol{\sigma}_{,\xi_i\xi_j} - (\nabla \cdot \mathbf{v})_{,\xi_j} \, \boldsymbol{\sigma}_{,\xi_i} \\ & + \nabla \mathbf{v}_{,\xi_i\xi_j} \, \boldsymbol{\sigma} + \nabla \mathbf{v}_{,\xi_i} \, \boldsymbol{\sigma}_{,\xi_j} + \nabla \mathbf{v} \, \boldsymbol{\sigma}_{,\xi_i\xi_j} + \nabla \mathbf{v}_{,\xi_j} \, \boldsymbol{\sigma}_{,\xi_i} \\ & + \boldsymbol{\sigma}_{,\xi_i\xi_j} \, \nabla \mathbf{v}^T + \boldsymbol{\sigma}_{,\xi_i} \, \nabla \mathbf{v}^T_{,\xi_j} + \boldsymbol{\sigma} \, \nabla \mathbf{v}^T_{,\xi_i\xi_j} + \boldsymbol{\sigma}_{,\xi_j} \, \nabla \mathbf{v}^T_{,\xi_i}, \end{aligned} \tag{13}$$

which is the evolution equation for the stress second gradient that is required to evaluate the third term in Equation (6).

2.2.1. Update Algorithms for the Cauchy Stress and Its Gradients

We apply a combination of operator-splitting and midpoint time integration approaches [36] to the ODEs given by Equations (11)-(13) to develop update algorithms for the stress and its gradients. This results in a classical half-step rotation approach for the stress update and the corresponding extensions to the stress gradients detailed in what follows.

Stress Update To update the stress, we carry out the following three-step procedure:

1. Rotate the Cauchy stress to the configuration at $t^{n+\frac{1}{2}}$:

$$\tilde{\boldsymbol{\sigma}}^n = \boldsymbol{\sigma}^n + \frac{\Delta t}{2}\left(-(\nabla \cdot \mathbf{v})^{n+\frac{1}{2}} \boldsymbol{\sigma}^n + \nabla \mathbf{v}^{n+\frac{1}{2}} \boldsymbol{\sigma}^n + \boldsymbol{\sigma}^n (\nabla \mathbf{v}^T)^{n+\frac{1}{2}}\right). \tag{14}$$

2. Update the Cauchy stress in the configuration at $t^{n+\frac{1}{2}}$ using a constitutive model:

$$\tilde{\boldsymbol{\sigma}}^{n+1} = \tilde{\boldsymbol{\sigma}}^n + \Delta\tilde{\boldsymbol{\sigma}}, \tag{15}$$

where the stress increment $\Delta\tilde{\boldsymbol{\sigma}}$ is given by

$$\Delta\tilde{\boldsymbol{\sigma}} = \Delta t\, \mathcal{H}(\tilde{\boldsymbol{\sigma}}^n, \nabla\mathbf{v}^{n+\frac{1}{2}}), \tag{16}$$

It is important to note that if a midpoint technique is used to integrate Equation (2) in time, only one half of the stress increment $\Delta\tilde{\boldsymbol{\sigma}}$ is added to $\tilde{\boldsymbol{\sigma}}^n$ to produce the stress field at time $t^{n+\frac{1}{2}}$ in order to compute the contributions of the internal force terms in Equation (6).

3. Rotate the updated Cauchy stress to the configuration at t^{n+1}:

$$\boldsymbol{\sigma}^{n+1} = \tilde{\boldsymbol{\sigma}}^{n+1} + \frac{\Delta t}{2}\left(-(\nabla \cdot \mathbf{v})^{n+\frac{1}{2}} \tilde{\boldsymbol{\sigma}}^{n+1} + \nabla\mathbf{v}^{n+\frac{1}{2}} \tilde{\boldsymbol{\sigma}}^{n+1} + \tilde{\boldsymbol{\sigma}}^{n+1} (\nabla\mathbf{v}^T)^{n+\frac{1}{2}}\right), \tag{17}$$

and store the result as the initial condition for the stress update in the next time step.

Stress Gradient Update For the stress gradient update, we carry out the following three-step procedure:

1. Rotate the Cauchy stress gradient to the configuration at $t^{n+\frac{1}{2}}$:

$$\begin{aligned}\tilde{\boldsymbol{\sigma}}^n_{,\xi_i} = \boldsymbol{\sigma}^n_{,\xi_i} + \frac{\Delta t}{2}\Big(&-(\nabla \cdot \mathbf{v})^{n+\frac{1}{2}}_{,\xi_i} \boldsymbol{\sigma}^n - (\nabla \cdot \mathbf{v})^{n+\frac{1}{2}} \boldsymbol{\sigma}^n_{,\xi_i}\\ &+ \nabla\mathbf{v}^{n+\frac{1}{2}}_{,\xi_i} \boldsymbol{\sigma}^n + \nabla\mathbf{v}^{n+\frac{1}{2}} \boldsymbol{\sigma}^n_{,\xi_i} + \boldsymbol{\sigma}^n_{,\xi_i} (\nabla\mathbf{v}^T)^{n+\frac{1}{2}} + \boldsymbol{\sigma}^n (\nabla\mathbf{v}^T_{,\xi_i})^{n+\frac{1}{2}}\Big).\end{aligned} \tag{18}$$

2. Update the Cauchy stress gradient in the configuration at $t^{n+\frac{1}{2}}$ using a constitutive model:

$$\tilde{\boldsymbol{\sigma}}^{n+1}_{,\xi_i} = \tilde{\boldsymbol{\sigma}}^n_{,\xi_i} + \Delta\tilde{\boldsymbol{\sigma}}_{,\xi_i}. \tag{19}$$

The stress gradient increment $\Delta\tilde{\boldsymbol{\sigma}}_{,\xi_i}$ may be computed as

$$\Delta\tilde{\boldsymbol{\sigma}}_{,\xi_i} \approx \frac{\partial\boldsymbol{\sigma}}{\partial\boldsymbol{\epsilon}}\Delta\boldsymbol{\epsilon}_{,\xi_i} = \Delta t\, \boldsymbol{C}\nabla^s\mathbf{v}^{n+\frac{1}{2}}_{,\xi_i}, \tag{20}$$

where $\boldsymbol{\epsilon}$ is the strain, $\Delta\boldsymbol{\epsilon} = \Delta t \nabla^s \mathbf{v}^{n+\frac{1}{2}}$ is the strain increment over the time interval (t^n, t^{n+1}), ∇^s is the symmetric gradient, and $\boldsymbol{C}$ is the material tangent stiffness. Note that the stress gradient increment is driven by the strain gradient increment, which, in turn, is computed as a product of the strain rate gradient and time step size. As in the case of the stress update, if a midpoint technique is used to integrate Equation (2) in time, only one half of the stress gradient increment $\Delta\tilde{\boldsymbol{\sigma}}_{,\xi_i}$ is added to $\tilde{\boldsymbol{\sigma}}^n_{,\xi_i}$ to produce the stress gradient field at time $t^{n+\frac{1}{2}}$ in order to compute the first-order correction contributions of the internal force terms in Equations (6).

3. Rotate the updated Cauchy stress gradient to the configuration at t^{n+1}:

$$
\begin{aligned}
\boldsymbol{\sigma}^{n+1}_{,\xi_i} = \tilde{\boldsymbol{\sigma}}^{n+1}_{,\xi_i} + \frac{\Delta t}{2}\Big(&- (\nabla \cdot \mathbf{v})^{n+\frac{1}{2}}_{,\xi_i} \boldsymbol{\sigma}^{n+1} - (\nabla \cdot \mathbf{v})^{n+\frac{1}{2}} \tilde{\boldsymbol{\sigma}}^{n+1}_{,\xi_i} \\
&+ \nabla\mathbf{v}^{n+\frac{1}{2}}_{,\xi_i} \boldsymbol{\sigma}^{n+1} + \nabla\mathbf{v}^{n+\frac{1}{2}} \tilde{\boldsymbol{\sigma}}^{n+1}_{,\xi_i} + \tilde{\boldsymbol{\sigma}}^{n+1}_{,\xi_i} (\nabla\mathbf{v}^T)^{n+\frac{1}{2}} + \boldsymbol{\sigma}^{n+1} (\nabla\mathbf{v}^T_{,\xi_i})^{n+\frac{1}{2}} \Big),
\end{aligned}
\tag{21}
$$

and store the result as the initial condition for the stress gradient update in the next time step.

Stress Second Gradient Update For the stress second gradient update, we carry out the following three-step procedure:

1. Rotate the Cauchy stress second gradient to the configuration at $t^{n+\frac{1}{2}}$:

$$
\begin{aligned}
\tilde{\boldsymbol{\sigma}}^n_{,\xi_i\xi_j} = \boldsymbol{\sigma}^n_{,\xi_i\xi_j} + \frac{\Delta t}{2}\Big(&- (\nabla \cdot \mathbf{v})^{n+\frac{1}{2}}_{,\xi_i\xi_j} \boldsymbol{\sigma}^n - (\nabla \cdot \mathbf{v})^{n+\frac{1}{2}}_{,\xi_i} \boldsymbol{\sigma}^n_{,\xi_j} - (\nabla \cdot \mathbf{v})^{n+\frac{1}{2}} \boldsymbol{\sigma}^n_{,\xi_i\xi_j} - (\nabla \cdot \mathbf{v})^{n+\frac{1}{2}}_{,\xi_j} \boldsymbol{\sigma}^n_{,\xi_i} \\
&+ \nabla\mathbf{v}^{n+\frac{1}{2}}_{,\xi_i\xi_j} \boldsymbol{\sigma}^n + \nabla\mathbf{v}^{n+\frac{1}{2}}_{,\xi_i} \boldsymbol{\sigma}^n_{,\xi_j} + \nabla\mathbf{v}^{n+\frac{1}{2}} \boldsymbol{\sigma}^n_{,\xi_i\xi_j} + \nabla\mathbf{v}^{n+\frac{1}{2}}_{,\xi_j} \boldsymbol{\sigma}^n_{,\xi_i} \\
&+ \boldsymbol{\sigma}^n_{,\xi_i\xi_j} (\nabla\mathbf{v}^T)^{n+\frac{1}{2}} + \boldsymbol{\sigma}^n_{,\xi_i} (\nabla\mathbf{v}^T)^{n+\frac{1}{2}}_{,\xi_j} + \boldsymbol{\sigma}^n (\nabla\mathbf{v}^T_{,\xi_i\xi_j})^{n+\frac{1}{2}} + \boldsymbol{\sigma}^n_{,\xi_j} (\nabla\mathbf{v}^T_{,\xi_i})^{n+\frac{1}{2}} \Big).
\end{aligned}
\tag{22}
$$

2. Update the Cauchy stress second gradient in the configuration at $t^{n+\frac{1}{2}}$ using a constitutive model:

$$
\tilde{\boldsymbol{\sigma}}^{n+1}_{,\xi_i\xi_j} = \tilde{\boldsymbol{\sigma}}^n_{,\xi_i\xi_j} + \Delta\tilde{\boldsymbol{\sigma}}_{,\xi_i\xi_j}.
\tag{23}
$$

The stress second gradient increment $\Delta\tilde{\boldsymbol{\sigma}}_{,\xi_i\xi_j}$ may be computed as

$$
\Delta\tilde{\boldsymbol{\sigma}}_{,\xi_i\xi_j} \approx \frac{\partial\boldsymbol{\sigma}}{\partial\boldsymbol{\epsilon}}\Delta\boldsymbol{\epsilon}_{,\xi_i\xi_j} = \Delta t\, \boldsymbol{C} \nabla^s \mathbf{v}^{n+\frac{1}{2}}_{,\xi_i\xi_j}.
\tag{24}
$$

As before, if a midpoint technique is used to integrate Equation (2) in time, only one half of the stress second gradient increment $\Delta\tilde{\boldsymbol{\sigma}}_{,\xi_i\xi_j}$ is added to $\tilde{\boldsymbol{\sigma}}^n_{,\xi_i\xi_j}$ to produce the stress second gradient field at time $t^{n+\frac{1}{2}}$ in order to compute the contributions of the second-order correction to the internal force terms in Equation (6).

3. Rotate the updated Cauchy stress second gradient to the configuration at t^{n+1}:

$$
\begin{aligned}
\boldsymbol{\sigma}^{n+1}_{,\xi_i\xi_j} = \tilde{\boldsymbol{\sigma}}^{n+1}_{,\xi_i\xi_j} + \frac{\Delta t}{2}\Big(& -(\nabla \cdot \mathbf{v})^{n+\frac{1}{2}}_{,\xi_i\xi_j} \boldsymbol{\sigma}^{n+1} - (\nabla \cdot \mathbf{v})^{n+\frac{1}{2}}_{,\xi_i} \boldsymbol{\sigma}^{n+1}_{,\xi_j} - (\nabla \cdot \mathbf{v})^{n+\frac{1}{2}} \tilde{\boldsymbol{\sigma}}^{n+1}_{,\xi_i\xi_j} - (\nabla \cdot \mathbf{v})^{n+\frac{1}{2}}_{,\xi_j} \boldsymbol{\sigma}^{n+1}_{,\xi_i} \\
& + \nabla \mathbf{v}^{n+\frac{1}{2}}_{,\xi_i\xi_j} \boldsymbol{\sigma}^{n+1} + \nabla \mathbf{v}^{n+\frac{1}{2}}_{,\xi_i} \boldsymbol{\sigma}^{n+1}_{,\xi_j} + \nabla \mathbf{v}^{n+\frac{1}{2}} \tilde{\boldsymbol{\sigma}}^{n+1}_{,\xi_i\xi_j} + \nabla \mathbf{v}^{n+\frac{1}{2}}_{,\xi_j} \boldsymbol{\sigma}^{n+1}_{,\xi_i} \\
& + \tilde{\boldsymbol{\sigma}}^{n+1}_{,\xi_i\xi_j} (\nabla \mathbf{v}^T)^{n+\frac{1}{2}} + \boldsymbol{\sigma}^{n+1}_{,\xi_i} (\nabla \mathbf{v}^T)^{n+\frac{1}{2}}_{,\xi_j} + \boldsymbol{\sigma}^{n+1} (\nabla \mathbf{v}^T_{,\xi_i\xi_j})^{n+\frac{1}{2}} + \boldsymbol{\sigma}^{n+1}_{,\xi_j} (\nabla \mathbf{v}^T_{,\xi_i})^{n+\frac{1}{2}} \Big),
\end{aligned}
$$

(25)

and store the result as the initial condition for the stress second gradient update in the next time step.

Remark 1. The theory presented in this work makes use of the Truesdell rate of the Cauchy stress, which is an objective rate that is also natural for constitutive models defined in terms of the Second Piola–Kirchhoff stress tensor, like in the case of hyperelasticity [35]. The proposed formulation can accommodate other objective rates, which will introduce minor changes in the evolution of the stress and its gradients. For example, the formulation based on the popular Jaumann rate of the Cauchy stress may be obtained by replacing the velocity gradient with with its skew-symmetric counterpart given by $\frac{1}{2}(\nabla \mathbf{v} - \nabla \mathbf{v}^T)$ (see also [36]).

Remark 2. The half-step algorithm above is second-order accurate in time and is used for the dynamic analyses shown in this work. As an alternative that is better suited for quasi-static simulations, a full-step approach may be adopted. In this case, the algorithms are reduced to two steps where a full-step rotation is followed by the material update. In that case, Equation (2) may be integrated in time using the Backward Euler method. Alternatively, the inertial terms may be dropped all together to produce a truly static response.

2.3. Linearization

For implicit computations using the Newton–Rhapson technique, the governing equations need to be linearized with respect to the solution unknowns, which, in the present formulation, are assumed to be nodal velocities at step $n+1$. We focus on the linearization of the internal force vector and separate the contributions to the left-hand-side matrix coming from one-point quadrature and correction terms as

$$
\mathbf{K} = \mathbf{K}^{1pt} + \mathbf{K}^{corr1} + \mathbf{K}^{corr2}.
$$

(26)

Here, $\mathbf{K}^{corr1}$ and $\mathbf{K}^{corr2}$ are the first-order and second-order correction contributions, respectively. The tangent stiffness matrix coming from the one-point quadrature term is standard and may be

expressed as

$$K_{AiBj}^{\text{1pt}} = \frac{\Delta t}{4}\left(J_\xi(\mathbf{0})\int_\square d\square\right)B_{AIi}(\mathbf{0})D_{IJ}(\mathbf{0})B_{BJj}(\mathbf{0})$$
$$+ \frac{\Delta t}{4}\left(J_\xi(\mathbf{0})\int_\square d\square\right)N_{A,x_k}(\mathbf{0})\sigma_{kl}(\mathbf{0})N_{B,x_l}(\mathbf{0})\delta_{ij}, \tag{27}$$

where the first and second term on the right hand side correspond to the material and geometric stiffness contributions, respectively, δ_{ij} is the Kronecker delta, and D_{IJ} are the components of the material tangent stiffness tensor $\mathcal{C}$ in the Voigt notation.

The left-hand-side matrix contributions coming from the first- and second-order correction terms may be deduced from the second and third terms, respectively, on the right-hand side of Equation (6) and expressed as:

$$K_{AiBj}^{\text{corr1}} = \frac{\Delta t}{4}\left(J_\xi(\mathbf{0})\int_\square \xi_k\xi_l d\square\right)B_{AIi,\xi_k}(\mathbf{0})D_{IJ}(\mathbf{0})B_{BJj,\xi_l}(\mathbf{0})$$
$$+ \frac{\Delta t}{4}\left(J_\xi(\mathbf{0})\int_\square \xi_m\xi_n d\square\right)N_{A,x_k\xi_m}(\mathbf{0})\sigma_{kl}(\mathbf{0})N_{B,x_l\xi_n}(\mathbf{0})\delta_{ij}, \tag{28}$$

and

$$K_{AiBj}^{\text{corr2}} = \frac{\Delta t}{16}\left(J_\xi(\mathbf{0})\int_\square \xi_k\xi_l\xi_m\xi_n d\square\right)B_{AIi,\xi_k\xi_l}(\mathbf{0})D_{IJ}(\mathbf{0})B_{BJj,\xi_m\xi_n}(\mathbf{0})$$
$$+ \frac{\Delta t}{16}\left(J_\xi(\mathbf{0})\int_\square \xi_p\xi_q\xi_r\xi_s d\square\right)N_{A,x_k\xi_p\xi_q}(\mathbf{0})\sigma_{kl}(\mathbf{0})N_{B,x_l\xi_r\xi_s}(\mathbf{0})\delta_{ij}, \tag{29}$$

where, as before, we separate the material and geometric stiffness contributions. In the above expressions the factor $\frac{\Delta t}{4}$ assumes the use of midpoint time integration and nodal velocities as unknowns.

Remark 3. The formulation presented in this section includes correction terms up to second order. It should be noted that for a 2D linear quadrilateral the contribution of the second-order correction terms is identically zero, which simplifies the formulation considerably. As pointed out in [1], for a 3D linear hexahedron, second-order correction includes a handful of non-zero terms that should be included in the formulation to eliminate zero-energy modes present the formulation using only first-order correction.

2.4. Treatment of Near-Incompressibility

It is well known that nearly incompressible materials exhibit volumetric locking under full quadrature, while low-order quadrature leads to hourglassing [9, 10, 41]. In addition, even compressible materials exhibit volumetric locking under full quadrature in the presence of plastic de-

formations, which are isochoric. As a result, the proposed correction framework needs to be modified to enable stable and accurate handling of near-incompressibility and plastic deformations. To develop the formulation, we take inspiration from the B-bar technique [37] and first carry out an additive decomposition of the strain-rate velocity matrix $\mathbf{B}_A$ into its deviatoric and dilatational parts as

$$\mathbf{B}_A = \mathbf{B}_A^{\mathrm{dev}} + \mathbf{B}_A^{\mathrm{dil}}, \tag{30}$$

where, in 3D,

$$\mathbf{B}_A^{\mathrm{dev}} = \begin{bmatrix} \frac{2}{3}N_{A,x_1} & -\frac{1}{3}N_{A,x_2} & -\frac{1}{3}N_{A,x_3} \\ -\frac{1}{3}N_{A,x_1} & \frac{2}{3}N_{A,x_2} & -\frac{1}{3}N_{A,x_3} \\ -\frac{1}{3}N_{A,x_1} & -\frac{1}{3}N_{A,x_2} & \frac{2}{3}N_{A,x_3} \\ 0 & N_{A,x_3} & N_{A,x_2} \\ N_{A,x_3} & 0 & N_{A,x_1} \\ N_{A,x_2} & N_{A,x_1} & 0 \end{bmatrix}, \tag{31}$$

and

$$\mathbf{B}_A^{\mathrm{dil}} = \begin{bmatrix} \frac{1}{3}N_{A,x_1} & \frac{1}{3}N_{A,x_2} & \frac{1}{3}N_{A,x_3} \\ \frac{1}{3}N_{A,x_1} & \frac{1}{3}N_{A,x_2} & \frac{1}{3}N_{A,x_3} \\ \frac{1}{3}N_{A,x_1} & \frac{1}{3}N_{A,x_2} & \frac{1}{3}N_{A,x_3} \\ 0 & 0 & 0 \\ 0 & 0 & 0 \\ 0 & 0 & 0 \end{bmatrix}. \tag{32}$$

We also provide the expressions for $\mathbf{B}_{A,\xi_i}^{\mathrm{dev}}$ and $\mathbf{B}_{A,\xi_i\xi_j}^{\mathrm{dev}}$, which we will use in the following sections:

$$\mathbf{B}_{A,\xi_i}^{\mathrm{dev}} = \begin{bmatrix} \frac{2}{3}N_{A,x_1\xi_i} & -\frac{1}{3}N_{A,x_2\xi_i} & -\frac{1}{3}N_{A,x_3\xi_i} \\ -\frac{1}{3}N_{A,x_1\xi_i} & \frac{2}{3}N_{A,x_2\xi_i} & -\frac{1}{3}N_{A,x_3\xi_i} \\ -\frac{1}{3}N_{A,x_1\xi_i} & -\frac{1}{3}N_{A,x_2\xi_i} & \frac{2}{3}N_{A,x_3\xi_i} \\ 0 & N_{A,x_3\xi_i} & N_{A,x_2\xi_i} \\ N_{A,x_3\xi_i} & 0 & N_{A,x_1\xi_i} \\ N_{A,x_2\xi_i} & N_{A,x_1\xi_i} & 0 \end{bmatrix}, \quad \mathbf{B}_{A,\xi_i\xi_j}^{\mathrm{dev}} = \begin{bmatrix} \frac{2}{3}N_{A,x_1\xi_i\xi_j} & -\frac{1}{3}N_{A,x_2\xi_i\xi_j} & -\frac{1}{3}N_{A,x_3\xi_i\xi_j} \\ -\frac{1}{3}N_{A,x_1\xi_i\xi_j} & \frac{2}{3}N_{A,x_2\xi_i\xi_j} & -\frac{1}{3}N_{A,x_3\xi_i\xi_j} \\ -\frac{1}{3}N_{A,x_1\xi_i\xi_j} & -\frac{1}{3}N_{A,x_2\xi_i\xi_j} & \frac{2}{3}N_{A,x_3\xi_i\xi_j} \\ 0 & N_{A,x_3\xi_i\xi_j} & N_{A,x_2\xi_i\xi_j} \\ N_{A,x_3\xi_i\xi_j} & 0 & N_{A,x_1\xi_i\xi_j} \\ N_{A,x_2\xi_i\xi_j} & N_{A,x_1\xi_i\xi_j} & 0 \end{bmatrix}. \tag{33}$$

As a next step, we develop $\bar{\mathbf{B}}_A$, the "bar" version of the strain rate-velocity matrix. We first present the lower-order case, suitable for linear FEM, and then show an extension to the higher-order case suitable for quadratic NURBS.

2.4.1. Low-Order Case

We project $\mathbf{B}_A^{\text{dil}}$ onto the integration-zone constants by interpolating it at the parametric origin as

$$\bar{\mathbf{B}}_A^{\text{dil}} = \mathbf{B}_A^{\text{dil}}(\mathbf{0}), \tag{34}$$

and define $\bar{\mathbf{B}}_A$ as

$$\bar{\mathbf{B}}_A = \mathbf{B}_A^{\text{dev}} + \bar{\mathbf{B}}_A^{\text{dil}} = \mathbf{B}_A^{\text{dev}} + \mathbf{B}_A^{\text{dil}}(\mathbf{0}). \tag{35}$$

Note that the above choice implies: i) $\bar{\mathbf{B}}_A(\mathbf{0}) = \mathbf{B}_A(\mathbf{0})$; and ii) $\bar{\mathbf{B}}_{A,\xi_i}(\mathbf{0}) = \mathbf{B}_{A,\xi_i}^{\text{dev}}(\mathbf{0})$ and $\bar{\mathbf{B}}_{A,\xi_i\xi_j}(\mathbf{0}) = \mathbf{B}_{A,\xi_i\xi_j}^{\text{dev}}(\mathbf{0})$. Replacing $\mathbf{B}_A$ with $\bar{\mathbf{B}}_A$ in the Galerkin formulation given by Equation (2) results in the following expressions for the internal force vector:

$$
\begin{aligned}
\int_{\Omega_e} \bar{\mathbf{B}}_A^T \boldsymbol{\sigma} \, d\Omega \approx{}& \left(J_\xi(\mathbf{0}) \int_\square d\square \right) \mathbf{B}_A^T(\mathbf{0})\boldsymbol{\sigma}(\mathbf{0}) \\
&+ \left(J_\xi(\mathbf{0}) \int_\square \xi_i\xi_j d\square \right) \mathbf{B}_{A,\xi_i}^{\text{dev}\,T}(\mathbf{0})\boldsymbol{\sigma}_{,\xi_j}(\mathbf{0}) \\
&+ \left(J_\xi(\mathbf{0}) \int_\square \xi_k\xi_l\xi_m\xi_n d\square \right) \mathbf{B}_{A,\xi_k\xi_l}^{\text{dev}\,T}(\mathbf{0})\boldsymbol{\sigma}_{,\xi_m\xi_n}(\mathbf{0}).
\end{aligned}
\tag{36}
$$

Here, the first- and second-order corrections make use of the deviatoric part of the stress, a key idea in development of the selective/reduced integration (SRI) schemes [42]. The tangent matrix corresponding to the above force vector may be now expressed as

$$\mathbf{K} = \mathbf{K}^{\text{1pt}} + \mathbf{K}^{\text{corr1}} + \mathbf{K}^{\text{corr2}}, \tag{37}$$

where the one-point quadrature contribution $\mathbf{K}^{\text{1pt}}$ is the same as in Equation (27) and the correction contributions are:

$$
\begin{aligned}
K_{AiBj}^{\text{corr1}} ={}& \frac{\Delta t}{4} \left(J_\xi(\mathbf{0}) \int_\square \xi_k\xi_l d\square \right) B_{Ali,\xi_k}^{\text{dev}}(\mathbf{0})D_{IJ}(\mathbf{0})B_{BJj,\xi_l}^{\text{dev}}(\mathbf{0}) \\
&+ \frac{\Delta t}{4} \left(J_\xi(\mathbf{0}) \int_\square \xi_p\xi_q d\square \right) N_{A,x_n\xi_p}(\mathbf{0}) \left(T_{klin}^{\text{dev}}\sigma_{lm}(\mathbf{0})T_{kmjo}^{\text{dev}} \right) N_{B,x_o\xi_q}(\mathbf{0})
\end{aligned}
\tag{38}
$$

and

$$
\begin{aligned}
K_{AiBj}^{\text{corr2}} ={}& \frac{\Delta t}{16} \left(J_\xi(\mathbf{0}) \int_\square \xi_k\xi_l\xi_m\xi_n d\square \right) B_{Ali,\xi_k\xi_l}^{\text{dev}}(\mathbf{0})D_{IJ}(\mathbf{0})B_{BJj,\xi_m\xi_n}^{\text{dev}}(\mathbf{0}) \\
&+ \frac{\Delta t}{16} \left(J_\xi(\mathbf{0}) \int_\square \xi_p\xi_q\xi_r\xi_s d\square \right) N_{A,x_n\xi_p\xi_q}(\mathbf{0}) \left(T_{klin}^{\text{dev}}\sigma_{lm}(\mathbf{0})T_{kmjo}^{\text{dev}} \right) N_{B,x_o\xi_r\xi_s}(\mathbf{0}).
\end{aligned}
\tag{39}
$$

Here, $T_{ijkl}^{\text{dev}} = \delta_{ik}\delta_{jl} - \frac{1}{3}\delta_{ij}\delta_{kl}$ is the fourth-rank deviator tensor.

The stress first and second gradient update algorithms are also modified to account for near-incompressibility as follows:

Stress Gradient Update The three-step stress gradient evolution algorithm becomes:

1. Rotate the Cauchy stress gradient to the configuration at $t^{n+\frac{1}{2}}$:

$$
\begin{aligned}
\tilde{\boldsymbol{\sigma}}^n_{,\xi_i} = \boldsymbol{\sigma}^n_{,\xi_i} + \frac{\Delta t}{2}\Big(&- (\nabla \cdot \mathbf{v})^{n+\frac{1}{2}}\, \boldsymbol{\sigma}^n_{,\xi_i} \\
&+ \nabla \mathbf{v}^{\mathrm{dev},n+\frac{1}{2}}_{,\xi_i}\, \boldsymbol{\sigma}^n + \nabla \mathbf{v}^{n+\frac{1}{2}}\, \boldsymbol{\sigma}^n_{,\xi_i} + \boldsymbol{\sigma}^n_{,\xi_i}\, (\nabla \mathbf{v}^T)^{n+\frac{1}{2}} + \boldsymbol{\sigma}^n\, (\nabla \mathbf{v}^T_{,\xi_i})^{\mathrm{dev},n+\frac{1}{2}} \Big).
\end{aligned}
\tag{40}
$$

2. Update the Cauchy stress gradient in the configuration at $t^{n+\frac{1}{2}}$ using:

$$
\tilde{\boldsymbol{\sigma}}^{n+1}_{,\xi_i} = \tilde{\boldsymbol{\sigma}}^n_{,\xi_i} + \Delta t\, \boldsymbol{C} \nabla^s \mathbf{v}^{\mathrm{dev},n+\frac{1}{2}}_{,\xi_i}.
\tag{41}
$$

3. Rotate the updated Cauchy stress gradient to the configuration at t^{n+1}:

$$
\begin{aligned}
\boldsymbol{\sigma}^{n+1}_{,\xi_i} = \tilde{\boldsymbol{\sigma}}^{n+1}_{,\xi_i} + \frac{\Delta t}{2}\Big(&- (\nabla \cdot \mathbf{v})^{n+\frac{1}{2}}\, \tilde{\boldsymbol{\sigma}}^{n+1}_{,\xi_i} \\
&+ \nabla \mathbf{v}^{\mathrm{dev},n+\frac{1}{2}}_{,\xi_i}\, \boldsymbol{\sigma}^{n+1} + \nabla \mathbf{v}^{n+\frac{1}{2}}\, \tilde{\boldsymbol{\sigma}}^{n+1}_{,\xi_i} + \tilde{\boldsymbol{\sigma}}^{n+1}_{,\xi_i}\, (\nabla \mathbf{v}^T)^{n+\frac{1}{2}} + \boldsymbol{\sigma}^{n+1}\, (\nabla \mathbf{v}^T_{,\xi_i})^{\mathrm{dev},n+\frac{1}{2}} \Big),
\end{aligned}
\tag{42}
$$

and store the result as the initial condition for the stress gradient update in the next time step. Note that in all the terms using parametric derivatives of the velocity gradient only its deviatoric part survives, hence the use of the dev superscript in Equations (40)-(42).

Stress Second Gradient Update The three-step stress second gradient evolution algorithm becomes:

1. Rotate the Cauchy stress second gradient to the configuration at $t^{n+\frac{1}{2}}$:

$$
\begin{aligned}
\tilde{\boldsymbol{\sigma}}^n_{,\xi_i\xi_j} = \boldsymbol{\sigma}^n_{,\xi_i\xi_j} + \frac{\Delta t}{2}\Big(&- (\nabla \cdot \mathbf{v})^{n+\frac{1}{2}}\, \boldsymbol{\sigma}^n_{,\xi_i\xi_j} \\
&+ \nabla \mathbf{v}^{\mathrm{dev},n+\frac{1}{2}}_{,\xi_i\xi_j}\, \boldsymbol{\sigma}^n + \nabla \mathbf{v}^{\mathrm{dev},n+\frac{1}{2}}_{,\xi_i}\, \boldsymbol{\sigma}^n_{,\xi_j} + \nabla \mathbf{v}^{n+\frac{1}{2}}\, \boldsymbol{\sigma}^n_{,\xi_i\xi_j} + \nabla \mathbf{v}^{\mathrm{dev},n+\frac{1}{2}}_{,\xi_j}\, \boldsymbol{\sigma}^n_{,\xi_i} \\
&+ \boldsymbol{\sigma}^n_{,\xi_i\xi_j}\, (\nabla \mathbf{v}^T)^{n+\frac{1}{2}} + \boldsymbol{\sigma}^n_{,\xi_i}\, (\nabla \mathbf{v}^T)^{\mathrm{dev},n+\frac{1}{2}}_{,\xi_j} + \boldsymbol{\sigma}^n\, (\nabla \mathbf{v}^T_{,\xi_i\xi_j})^{\mathrm{dev},n+\frac{1}{2}} + \boldsymbol{\sigma}^n_{,\xi_j}\, (\nabla \mathbf{v}^T_{,\xi_i})^{\mathrm{dev},n+\frac{1}{2}} \Big).
\end{aligned}
\tag{43}
$$

2. Update the Cauchy stress second gradient in the configuration at $t^{n+\frac{1}{2}}$ using:

$$
\tilde{\boldsymbol{\sigma}}^{n+1}_{,\xi_i\xi_j} = \tilde{\boldsymbol{\sigma}}^n_{,\xi_i\xi_j} + \Delta t\, \boldsymbol{C} \nabla^s \mathbf{v}^{\mathrm{dev},n+\frac{1}{2}}_{,\xi_i\xi_j}.
\tag{44}
$$

13

3. Rotate the updated Cauchy stress second gradient to the configuration at t^{n+1}:

$$
\begin{aligned}
\boldsymbol{\sigma}^{n+1}_{,\xi_i\xi_j} = {} & \tilde{\boldsymbol{\sigma}}^{n+1}_{,\xi_i\xi_j} + \frac{\Delta t}{2}\Big(-(\nabla \cdot \mathbf{v})^{n+\frac{1}{2}}\, \tilde{\boldsymbol{\sigma}}^{n+1}_{,\xi_i\xi_j} \\
& + \nabla\mathbf{v}^{\mathrm{dev},n+\frac{1}{2}}_{,\xi_i\xi_j}\, \boldsymbol{\sigma}^{n+1} + \nabla\mathbf{v}^{\mathrm{dev},n+\frac{1}{2}}_{,\xi_i}\, \boldsymbol{\sigma}^{n+1}_{,\xi_j} + \nabla\mathbf{v}^{n+\frac{1}{2}}\, \tilde{\boldsymbol{\sigma}}^{n+1}_{,\xi_i\xi_j} + \nabla\mathbf{v}^{\mathrm{dev},n+\frac{1}{2}}_{,\xi_j}\, \boldsymbol{\sigma}^{n+1}_{,\xi_i} \\
& + \tilde{\boldsymbol{\sigma}}^{n+1}_{,\xi_i\xi_j}\, (\nabla\mathbf{v}^T)^{n+\frac{1}{2}} + \boldsymbol{\sigma}^{n+1}_{,\xi_i}\, (\nabla\mathbf{v}^T)^{\mathrm{dev},n+\frac{1}{2}}_{,\xi_j} + \boldsymbol{\sigma}^{n+1}\, (\nabla\mathbf{v}^T_{,\xi_i\xi_j})^{\mathrm{dev},n+\frac{1}{2}} + \boldsymbol{\sigma}^{n+1}_{,\xi_j}\, (\nabla\mathbf{v}^T_{,\xi_i})^{\mathrm{dev},n+\frac{1}{2}}\Big),
\end{aligned}
\tag{45}
$$

and store the result as the initial condition for the stress second gradient update in the next time step.

2.4.2. Higher-Order Case

To achieve better accuracy and stability for higher-order elements (e.g., quadratic NURBS) we expand $\mathbf{B}_A^{\mathrm{dil}}$ in Taylor series to include the linear modes as

$$
\bar{\mathbf{B}}_A^{\mathrm{dil}} = \mathbf{B}_A^{\mathrm{dil}}(\mathbf{0}) + \xi_j \mathbf{B}_{A,\xi_j}^{\mathrm{dil}}(\mathbf{0}),
\tag{46}
$$

and define $\bar{\mathbf{B}}_A$ as

$$
\bar{\mathbf{B}}_A = \mathbf{B}_A^{\mathrm{dev}} + \bar{\mathbf{B}}_A^{\mathrm{dil}} = \mathbf{B}_A^{\mathrm{dev}} + \mathbf{B}_A^{\mathrm{dil}}(\mathbf{0}) + \xi_j \mathbf{B}_{A,\xi_j}^{\mathrm{dil}}(\mathbf{0}).
\tag{47}
$$

This choice implies: i) $\bar{\mathbf{B}}_A(\mathbf{0}) = \mathbf{B}_A(\mathbf{0})$ and $\bar{\mathbf{B}}_{A,\xi_i}(\mathbf{0}) = \mathbf{B}_{A,\xi_i}(\mathbf{0})$; and ii) $\bar{\mathbf{B}}_{A,\xi_i\xi_j}(\mathbf{0}) = \mathbf{B}_{A,\xi_i\xi_j}^{\mathrm{dev}}(\mathbf{0})$. Replacing $\mathbf{B}_A$ with $\bar{\mathbf{B}}_A$ in the Galerkin formulation given by Equation (2) gives the following expressions for the internal force vector:

$$
\begin{aligned}
\int_{\Omega_e} \mathbf{B}_A^T \boldsymbol{\sigma}\, d\Omega \approx {} & \left(J_\xi(\mathbf{0}) \int_\square d\square \right) \mathbf{B}_A^T(\mathbf{0})\boldsymbol{\sigma}(\mathbf{0}) \\
& + \left(J_\xi(\mathbf{0}) \int_\square \xi_i\xi_j d\square \right) \mathbf{B}_{A,\xi_i}^T(\mathbf{0})\boldsymbol{\sigma}_{,\xi_j}(\mathbf{0}) \\
& + \left(\frac{J_\xi(\mathbf{0})}{4} \int_\square \xi_k\xi_l\xi_m\xi_n d\square \right) \mathbf{B}_{A,\xi_k\xi_l}^{\mathrm{dev}\,T}(\mathbf{0})\boldsymbol{\sigma}_{,\xi_m\xi_n}(\mathbf{0}).
\end{aligned}
\tag{48}
$$

Note that in this construction the one-point quadrature and first-order correction terms make use of the full stress, while the second-order correction terms make use of the deviatoric part of the stress. The tangent-matrix contributions for the one-point quadrature and first-order correction terms are thus given by Equations (27) and (28), respectively, while Equation (39) is employed to compute the tangent-matrix contributions of the second-order correction terms. Likewise, only the stress second gradient update algorithm needs to be modified to account for near-incompressibility.

2.4.3. Reduction to 2D

The reduction to 2D with treatment of near-incompressibility may be accomplished in two ways. Starting from the 2D definition of the strain rate - velocity matrix, we define its deviatoric

and dilatational parts as follows:

$$\mathbf{B}_A = \begin{bmatrix} N_{A,x_1} & 0 \\ 0 & N_{A,x_2} \\ N_{A,x_2} & N_{A,x_1} \end{bmatrix}, \tag{49}$$

$$\mathbf{B}_A^{\text{dev}} = \begin{bmatrix} \frac{1}{2}N_{A,x_1} & -\frac{1}{2}N_{A,x_2} \\ -\frac{1}{2}N_{A,x_1} & \frac{1}{2}N_{A,x_2} \\ N_{A,x_2} & N_{A,x_1} \end{bmatrix}, \tag{50}$$

and

$$\mathbf{B}_A^{\text{dil}} = \begin{bmatrix} \frac{1}{2}N_{A,x_1} & \frac{1}{2}N_{A,x_2} \\ \frac{1}{2}N_{A,x_1} & \frac{1}{2}N_{A,x_2} \\ 0 & 0 \end{bmatrix}. \tag{51}$$

In addition, the parametric gradient of $\mathbf{B}_A^{\text{dev}}$ becomes

$$\mathbf{B}_{A,\xi_i}^{\text{dev}} = \begin{bmatrix} \frac{1}{2}N_{A,x_1\xi_i} & -\frac{1}{2}N_{A,x_2\xi_i} \\ -\frac{1}{2}N_{A,x_1\xi_i} & \frac{1}{2}N_{A,x_2\xi_i} \\ N_{A,x_2\xi_i} & N_{A,x_1\xi_i} \end{bmatrix}. \tag{52}$$

Alternatively, starting with a 3D definition of the strain rate - velocity matrix, decomposing it into the deviatoric and dilatational parts, and then introducing the plane strain assumption (i.e., velocities in the x_3-direction and derivatives with respect to x_3 are set to zero) yields:

$$\mathbf{B}_A = \begin{bmatrix} N_{A,x_1} & 0 \\ 0 & N_{A,x_2} \\ 0 & 0 \\ N_{A,x_2} & N_{A,x_1} \end{bmatrix}, \tag{53}$$

$$\mathbf{B}_A^{\text{dev}} = \begin{bmatrix} \frac{2}{3}N_{A,x_1} & -\frac{1}{3}N_{A,x_2} \\ -\frac{1}{3}N_{A,x_1} & \frac{2}{3}N_{A,x_2} \\ -\frac{1}{3}N_{A,x_1} & -\frac{1}{3}N_{A,x_2} \\ N_{A,x_2} & N_{A,x_1} \end{bmatrix}, \tag{54}$$

and

$$\mathbf{B}_A^{\text{dil}} = \begin{bmatrix} \frac{1}{3}N_{A,x_1} & \frac{1}{3}N_{A,x_2} \\ \frac{1}{3}N_{A,x_1} & \frac{1}{3}N_{A,x_2} \\ \frac{1}{3}N_{A,x_1} & \frac{1}{3}N_{A,x_2} \\ 0 & 0 \end{bmatrix}. \tag{55}$$

Note that the top three rows of the matrices correspond to the axial strain-rate components and the 33 component of the strain rate is retained. The parametric gradient of $\mathbf{B}_A^{\text{dev}}$ now becomes

$$\mathbf{B}_{A,\xi_i}^{\text{dev}} = \begin{bmatrix} \frac{2}{3}N_{A,x_1\xi_i} & -\frac{1}{3}N_{A,x_2\xi_i} \\ -\frac{1}{3}N_{A,x_1\xi_i} & \frac{2}{3}N_{A,x_2\xi_i} \\ -\frac{1}{3}N_{A,x_1\xi_i} & -\frac{1}{3}N_{A,x_2\xi_i} \\ N_{A,x_2\xi_i} & N_{A,x_1\xi_i} \end{bmatrix}. \tag{56}$$

Looking at the internal force and tangent matrix given by Equations (36)-(38), both alternatives produce identical contributions for the one-point quadrature terms, while the contributions from the correction terms employing $\mathbf{B}_{A,\xi_i}^{\text{dev}}$ differ between the two approaches. We will study the effect of choosing one approach over the other in the Numerical Examples sections of the present paper.

3. Application to Specific Constitutive Models

In this section we provide details of the correction framework for a selection of constitutive material models, starting with hyperelastcity, progressing to Von Mises plasticity, and culminating with the M7 Microplane model of concrete failure. The latter is taken as an example of a complex material model treated as a "black box" algorithm in the present approach. (The M7 Microplane model [43] is available as a FORTRAN77 routine at[1].)

3.1. Hyperelasticity

Hyperelastic models assume the existence of a stored energy density function $\phi(\mathbf{E})$, where $\mathbf{E} = \frac{1}{2}(\mathbf{F}^T\mathbf{F} - \mathbf{I})$ is the Green–Lagrange strain and $\mathbf{F}$ is the deformation gradient. In this setting, the second Piola–Kirchhoff stress $\mathbf{S}$, which is work-conjugate to the Green–Lagrange strain, is obtained from the energy density function by taking its derivative with respect to the Green–Lagrange strain as $\mathbf{S} = \frac{\partial\phi}{\partial\mathbf{E}}$. The transformation between the second Piola–Kirchhoff and Cauchy stress takes on the following form:

$$\boldsymbol{\sigma} = J^{-1}\mathbf{F}\mathbf{S}\mathbf{F}^T, \tag{57}$$

where $J = \det\mathbf{F}$ is the determinant of the deformation gradient. The reader is referred to [44] and references therein for the background. Taking the material time derivative on both sides of Equation (57) and using the fact that $\dot{\mathbf{F}} = (\nabla\mathbf{v})\mathbf{F}$, results in the following expression for the material time derivative of the Cauchy stress:

$$\dot{\boldsymbol{\sigma}} = J^{-1}\mathbf{F}\dot{\mathbf{S}}\mathbf{F}^T - (\nabla \cdot \mathbf{v})\boldsymbol{\sigma} + \nabla\mathbf{v}\,\boldsymbol{\sigma} + \boldsymbol{\sigma}\,\nabla\mathbf{v}^T. \tag{58}$$

---

[1]http://www.civil.northwestern.edu/people/bazant/m7-coding/m7_cyc_schell_v1.f

Comparing Equations (11), (10) and (58), we immediately recognize that the Truesdell rate of the Cauchy stress may be expressed as a function of the material time derivative of the second Piola–Kirchhoff stress as

$$\dot{\boldsymbol{\sigma}}^{\mathrm{Tr}} = \mathcal{H}(\boldsymbol{\sigma}, \nabla \mathbf{v}) = J^{-1} \mathbf{F} \dot{\mathbf{S}} \mathbf{F}^T. \tag{59}$$

In addition, it is clear from the above derivations that the Truesdell rate naturally arises in the rate-form equations of hyperelasticity.

A direct computation of the material time derivative of $\mathbf{S}$ yields

$$\dot{\mathbf{S}} = \frac{\dot{\partial \phi}}{\partial \mathbf{E}} = \frac{\partial^2 \phi}{\partial \mathbf{E} \partial \mathbf{E}} \dot{\mathbf{E}} = \mathbf{C}^{\mathrm{he}} \dot{\mathbf{E}}, \tag{60}$$

where $\mathbf{C}^{\mathrm{he}} = \frac{\partial^2 \phi}{\partial \mathbf{E} \partial \mathbf{E}}$ is the material tangent tensor in the reference configuration. A direct computation of the material time derivative of $\mathbf{E}$ yields

$$\dot{\mathbf{E}} = \mathbf{F}^T \, \nabla^s \mathbf{v} \, \mathbf{F}. \tag{61}$$

Combining Equations (59)-(61) enables us to express the Truesdell rate of the Cauchy stress purely in terms of the current-configuration quantities as

$$\dot{\boldsymbol{\sigma}}^{\mathrm{Tr}} = \boldsymbol{\mathcal{C}}^{\mathrm{he}} \, \nabla^s \mathbf{v}, \tag{62}$$

where $\boldsymbol{\mathcal{C}}^{\mathrm{he}}$ is the current-configuration hyperelastic material tangent stiffness tensor. The latter is obtained from its reference-configuration counterpart $\mathbf{C}^{\mathrm{he}}$ and may be conveniently expressed in the index notation as

$$\mathcal{C}^{\mathrm{he}}_{ijkl} = J^{-1} F_{i\alpha} F_{j\beta} F_{k\gamma} F_{l\delta} \mathbf{C}^{\mathrm{he}}_{\alpha\beta\gamma\delta}, \tag{63}$$

where the Greek indices are used to denote the reference-configuration quantities. Using the material tangent stiffness from Equation (63) the increments of the stress and stress gradients may now be computed in a straightforward manner as

$$\Delta \tilde{\boldsymbol{\sigma}} = \Delta t \, \boldsymbol{\mathcal{C}}^{\mathrm{he}, n+\frac{1}{2}} \, \nabla^s \mathbf{v}^{n+\frac{1}{2}}, \tag{64}$$

$$\Delta \tilde{\boldsymbol{\sigma}}_{,\xi_i} \approx \Delta t \, \boldsymbol{\mathcal{C}}^{\mathrm{he}, n+\frac{1}{2}} \, \nabla^s \mathbf{v}^{n+\frac{1}{2}}_{,\xi_i}, \tag{65}$$

and

$$\Delta \tilde{\boldsymbol{\sigma}}_{,\xi_i \xi_j} \approx \Delta t \, \boldsymbol{\mathcal{C}}^{\mathrm{he}, n+\frac{1}{2}} \, \nabla^s \mathbf{v}^{n+\frac{1}{2}}_{,\xi_i \xi_j}, \tag{66}$$

To account for near-incompressibility, the latter updates are modified as

$$\Delta \tilde{\boldsymbol{\sigma}}_{,\xi_i} \approx \Delta t \, \boldsymbol{C}^{\text{he},n+\frac{1}{2}} \, \nabla^s \mathbf{v}^{\text{dev},n+\frac{1}{2}}_{,\xi_i} \tag{67}$$

and

$$\Delta \tilde{\boldsymbol{\sigma}}_{,\xi_i \xi_j} \approx \Delta t \, \boldsymbol{C}^{\text{he},n+\frac{1}{2}} \, \nabla^s \mathbf{v}^{\text{dev},n+\frac{1}{2}}_{,\xi_i \xi_j}. \tag{68}$$

For the Neo-Hookean solid used in the numerical examples section, the 3D stored energy density function ϕ may be written as

$$\phi(J, \mathbf{C}) = \phi^{\text{iso}}(\mathbf{C}) + \phi^{\text{vol}}(J), \tag{69}$$

where ϕ^{iso} and ϕ^{vol} are given by

$$\phi^{\text{iso}}(\mathbf{C}) = \frac{1}{2}\mu(\text{tr } \mathbf{C} - 3), \tag{70}$$

$$\phi^{\text{vol}}(J) = -\mu \ln J + \frac{1}{2}\kappa (\ln J)^2, \tag{71}$$

and $\mathbf{C} = 2\mathbf{E} + \mathbf{I}$ is the Cauchy–Green deformation tensor. With these definitions, the second Piola—Kirchhoff stress $\mathbf{S}$ becomes

$$\mathbf{S} = 2\frac{\partial \phi}{\partial \mathbf{C}} = \kappa \ln J \mathbf{C}^{-1} - \mu \mathbf{C}^{-1} + \mu \mathbf{I}, \tag{72}$$

while the reference-configuration material tangent stiffness tensor $\mathbf{C}^{\text{he}}$ is given by

$$\mathbf{C}^{\text{he}} = 4\frac{\partial^2 \phi}{\partial \mathbf{C} \partial \mathbf{C}} = 2(-\mu + \kappa \ln J)\frac{\partial \mathbf{C}^{-1}}{\partial \mathbf{C}} + \kappa \mathbf{C}^{-1} \otimes \mathbf{C}^{-1}. \tag{73}$$

Using the identity $\frac{\partial}{\partial \mathbf{C}}(\mathbf{C}^{-1}) : \mathbf{T} = -\mathbf{C}^{-1}\mathbf{T}\mathbf{C}^{-1}$, which holds for an arbitrary fourth-rank tensor $\mathbf{T}$, we can express the tangent stiffness tensor in the index notation as

$$C^{\text{he}}_{\alpha\beta\gamma\delta} = \kappa C^{-1}_{\alpha\beta} C^{-1}_{\gamma\delta} + (\mu - \kappa \ln J)(C^{-1}_{\alpha\gamma} C^{-1}_{\beta\delta} + C^{-1}_{\alpha\delta} C^{-1}_{\beta\gamma}). \tag{74}$$

Remark 4. Rather than using the rate form of hyperelasticity given by Equation (62), one may choose to evaluate the Cauchy stress directly by using Equation (57). In this case, the direct evaluation would apply to the one-point quadrature terms, while the stress gradients would be handled in the rate form with the updates given by Equations (65)-(66) or (67)-(68) for near-incompressibility.

3.2. Von Mises Isotropic Plasticity

We assume an isotropic hypoelastic-plastic material response of the form

$$\dot{\boldsymbol{\sigma}}^{\mathrm{Tr}} = \boldsymbol{C}^{\mathrm{el}} \left(\nabla^s \mathbf{v} - \nabla^s \mathbf{v}^{\mathrm{pl}} \right), \tag{75}$$

where $\nabla^s \mathbf{v}^{\mathrm{pl}}$ is the plastic strain rate and $\boldsymbol{C}^{\mathrm{el}}$ is the elastic stiffness tensor given by

$$C^{\mathrm{el}}_{ijkl} = \lambda \delta_{ij} \delta_{kl} + \mu \left(\delta_{ik} \delta_{jl} + \delta_{il} \delta_{jk} \right), \tag{76}$$

with λ and μ being the standard Lamé parameters. The von Mises yield criterion is defined through the yield function f as

$$f \left(\sigma^{\mathrm{vm}}, \overline{\epsilon}^p \right) = \sigma^{\mathrm{vm}} - \sigma_Y \left(\overline{\epsilon}^p \right), \tag{77}$$

where σ^{vm} is the von Mises stress, σ_Y is the yield stress, which is function of the equivalent plastic strain $\overline{\epsilon}^p$.

The yield function is employed as follows: The material responds elastically if $f \left(\sigma^{\mathrm{vm}}, \overline{\epsilon}^p \right) \leq 0$; plastic flow occurs on the so-called yield surface, i.e., for $f \left(\sigma^{\mathrm{vm}}, \overline{\epsilon}^p \right) = 0$; the yield function cannot exceed zero. To satisfy these conditions a return mapping technique was developed, which consists of the elastic predictor followed by, if necessary, the plastic corrector. The plastic corrector modifies the stress state and the associated internal variables to make sure the key yield condition, $f \left(\sigma^{\mathrm{vm}}, \overline{\epsilon}^p \right) = 0$, is satisfied. In the case of von Mises plasticity, the return mapping technique is known as the radial return algorithm [35].

The first step of the radial return algorithm consists of the elastic predictor that defines the trial Cauchy stress as

$$\boldsymbol{\sigma}^{\mathrm{trial}} = \boldsymbol{\sigma}^n + \Delta t \, \boldsymbol{C}^{\mathrm{el}} \, \nabla^s \mathbf{v}^{n+\frac{1}{2}}. \tag{78}$$

The deviatoric part of the trial stress is computed in the usual manner as

$$\boldsymbol{\sigma}^{\mathrm{dev}} = \boldsymbol{\sigma}^{\mathrm{trial}} - \frac{1}{3} (\mathrm{tr} \, \boldsymbol{\sigma}^{\mathrm{trial}}) \mathbf{I}, \tag{79}$$

and the trial von Mises stress becomes

$$\sigma^{\mathrm{vm}} = \sqrt{\frac{3}{2} \boldsymbol{\sigma}^{\mathrm{dev}} : \boldsymbol{\sigma}^{\mathrm{dev}}}. \tag{80}$$

If the trial von Mises stress is such that $f \left(\sigma^{\mathrm{vm}}, \overline{\epsilon}^p \right) \leq 0$, we conclude that the material response for that step is elastic and complete the update of the stress and its gradients using the elastic predictor as

$$\Delta \tilde{\boldsymbol{\sigma}} = \boldsymbol{\sigma}^{\mathrm{trial}} - \boldsymbol{\sigma}^n, \tag{81}$$

19

$$\Delta \tilde{\boldsymbol{\sigma}}_{,\xi_i} \approx \Delta t \, \boldsymbol{C}^{\mathrm{el}} \, \nabla^s \mathbf{v}_{,\xi_i}^{n+\frac{1}{2}}, \tag{82}$$

and

$$\Delta \tilde{\boldsymbol{\sigma}}_{,\xi_i\xi_j} \approx \Delta t \, \boldsymbol{C}^{\mathrm{el}} \, \nabla^s \mathbf{v}_{,\xi_i\xi_j}^{n+\frac{1}{2}}. \tag{83}$$

To account for near-incompressibility, the stress gradient updates become

$$\Delta \tilde{\boldsymbol{\sigma}}_{,\xi_i} \approx \Delta t \, \boldsymbol{C}^{\mathrm{el}} \, \nabla^s \mathbf{v}_{,\xi_i}^{\mathrm{dev},n+\frac{1}{2}}. \tag{84}$$

and

$$\Delta \tilde{\boldsymbol{\sigma}}_{,\xi_i\xi_j} \approx \Delta t \, \boldsymbol{C}^{\mathrm{el}} \, \nabla^s \mathbf{v}_{,\xi_i\xi_j}^{\mathrm{dev},n+\frac{1}{2}}. \tag{85}$$

If the trial von Mises stress is such that $f(\sigma^{\mathrm{vm}}, \overline{\epsilon}^p) > 0$, we radially return to the yield surface. For this, using Newton's method, we solve for the plastic strain increment $\Delta\gamma$ that satisfies the equation

$$f^*(\Delta\gamma) = \sigma^{\mathrm{vm}} - 3\mu\Delta\gamma - \sigma_Y(\overline{\epsilon}^{n,p} + \Delta\gamma) = 0. \tag{86}$$

Each step of the Newton iteration looks like

$$\Delta\gamma^{k+1} = \Delta\gamma^k + \frac{f^*(\Delta\gamma^k)}{3\mu + H^k}, \tag{87}$$

where k is the iteration counter and $H^k = \frac{d\sigma_Y}{d\overline{\epsilon}^p}$ is the hardening modulus at the kth iteration. Once the yield condition is met, we update the stress tensor and equivalent plastic strain as

$$\begin{aligned}
\boldsymbol{\sigma}^{n+1} &= \frac{1}{3}(\mathrm{tr}\,\boldsymbol{\sigma}^{\mathrm{trial}})\mathbf{I} + \left(1 - \frac{3\mu\Delta\gamma}{\sigma^{\mathrm{vm}}}\right)\boldsymbol{\sigma}^{\mathrm{dev}}, \\
\overline{\epsilon}^{n+1,p} &= \overline{\epsilon}^{n,p} + \Delta\gamma,
\end{aligned} \tag{88}$$

and compute the consistent elasto-plastic tangent modulus $\boldsymbol{C}^{\mathrm{ep}}$ [45] as

$$\begin{aligned}
C_{ijkl}^{\mathrm{ep}} &= \left(\lambda + \frac{2\mu}{3}\right)\delta_{ij}\delta_{kl} + 2\mu\beta I_{ijkl}^{\mathrm{dev}} - 2\mu\overline{\gamma}\,n_{ij}\,n_{kl} \\
\beta &= \frac{\sigma_Y}{\sigma^{\mathrm{vm}0}}, \quad \overline{\gamma} = \frac{1}{1 + \left(\frac{H}{3\mu}\right)} - (1 - \beta), \quad n_{ij} = \frac{\sigma_{ij}^{\mathrm{dev}}}{\sqrt{\sigma_{kl}^{\mathrm{dev}}\sigma_{kl}^{\mathrm{dev}}}},
\end{aligned} \tag{89}$$

where $I_{ijkl}^{\mathrm{dev}} = \frac{1}{2}\left(\delta_{ik}\delta_{jl} + \delta_{il}\delta_{jk}\right) - \frac{1}{3}\delta_{ij}\delta_{kl}$ is the symmetric fourth-rank deviatoric tensor. The stress and stress gradients are now updated using the results of the plastic corrector step as

$$\Delta\tilde{\boldsymbol{\sigma}} = \boldsymbol{\sigma}^{n+1} - \boldsymbol{\sigma}^n, \tag{90}$$

$$\Delta \tilde{\boldsymbol{\sigma}}_{,\xi_i} \approx \Delta t \, \boldsymbol{C}^{\mathrm{ep}} \, \nabla^s \mathbf{v}_{,\xi_i}^{n+\frac{1}{2}}, \tag{91}$$

and

$$\Delta \tilde{\boldsymbol{\sigma}}_{,\xi_i \xi_j} \approx \Delta t \, \boldsymbol{C}^{\mathrm{ep}} \, \nabla^s \mathbf{v}_{,\xi_i \xi_j}^{n+\frac{1}{2}}, \tag{92}$$

or, to account for near-incompressibility, as

$$\Delta \tilde{\boldsymbol{\sigma}}_{,\xi_i} \approx \Delta t \, \boldsymbol{C}^{\mathrm{ep}} \, \nabla^s \mathbf{v}_{,\xi_i}^{\mathrm{dev},n+\frac{1}{2}} \tag{93}$$

and

$$\Delta \tilde{\boldsymbol{\sigma}}_{,\xi_i \xi_j} \approx \Delta t \, \boldsymbol{C}^{\mathrm{ep}} \, \nabla^s \mathbf{v}_{,\xi_i \xi_j}^{\mathrm{dev},n+\frac{1}{2}}. \tag{94}$$

As will be shown in the numerical examples section, the latter stress gradient updates are critical to avoid volumetric locking associated with the volume-preserving plastic deformations, even if the material itself is compressible.

3.3. Approximate Material Tangent and the M7 Microplane Model of Concrete Failure

For more general constitutive models it is often the case that while the stress update is available, the material tangent stiffness, which is required for the first- and second-order correction terms is often too complex to derive analytically. In this case, we propose to approximate the material tangent stiffness using a finite-difference approach. The key idea and a detailed discussion of this technique may be traced back to [46].

We use Voigt notation in 3D and assume that the stress increment is obtained via a function or algorithm that takes the strain increment as input, i.e.,

$$\Delta \boldsymbol{\sigma} = \Delta \boldsymbol{\sigma}(\Delta \boldsymbol{\epsilon}). \tag{95}$$

To evaluate the tangent stiffness, we first define the strain vector increment in the direction J as $\Delta \boldsymbol{\epsilon}_J = \varepsilon \mathbf{e}_J$, where ε is a small number, $\mathbf{e}_J$ is a the Jth cartesian basis vector, and $J = 1, \ldots, 6$. The components of the tangent stiffness D_{IJ}, $I = 1, \ldots, 6$, are given by

$$D_{IJ} = \lim_{\varepsilon \to 0} \frac{\Delta \sigma_I(\Delta \boldsymbol{\epsilon}_J)}{\varepsilon}. \tag{96}$$

In practice, the limit is never taken and the above finite-difference-like expression in the present work is evaluated using $\varepsilon \leq 10^{-4}$. Note that in order to populate the tangent stiffness tensor entries the stress update function using the strain increment perturbations is called six times.

Remark 5. It is important that the tangent stiffness approximated by the above finite-difference formula is consistent with the stress state coming from the actual stress update. If the yield condi-

tion is met (not met) during the stress update, it must be assumed that the yield condition is also met (not met) for all the strain perturbations used in the finite-difference approximation of D_{IJ}.

We apply the above construction in the context of the M7 Miroplane Model of concrete failure the basics of which we summarize in what follows. The M7 model is the latest in a sequence of concrete models (labeled M0, M1, etc.) whose development began in the early 80s [39, 47–53]. A detailed history of these developments is provided in [39, 51]. In the microplane models, the material response occurs on a multitude of planes of different orientations with the vectorial strain and stress measures corresponding to a normal and two tangential (or shear) directions. This helps the physical insight of the modeler by intuitively reflecting the microcrack openings, shear slip and frictional dilatancy.

To characterize inelasticity or damage, the microplane stresses are subjected to the so-called stress-strain boundaries, which are the strain-dependent yield limits imposed on each microplane shown in [49, 50] to be appropriate for modeling of complex loading paths and load cycles. To incrementally update the vectorial stresses, a 12-step algorithm detailed in [39] is employed. The computational method involves an elastic predictor followed by a return (or drop) to the boundary at constant strain (similar to the classical radial return algorithm in plasticity). Once the microplane stresses are computed, the local tensorial stress is evaluated by employing the principle of virtual work and using the collection of all the vectorial stresses on each microplane (all the planes in different orientations on the surface of a unit hemisphere) [39]. The integral over the unit hemisphere is approximated using numerical integration [48]. As shown in [54], utilizing at least 37 microplanes is essential for maintaining accuracy.

The M7 model was further extend to implicit analysis in [43], where a tangent stiffness was derived. Here we approximate the material tangent stiffness using our finite difference approach and use the analytical version for comparison in the Numerical Examples section.

4. Numerical Examples

We first provide abbreviations of the methods employed in the examples presented in this section: FI stands for full integration; 1P1C stands for one point integration with correction up to first order; 1P1C-23INC is 1P1C with near-incompressibility treatment using the 2x3 B-matrix in 2D (see Section 2.4.3); 1P1C-24INC is 1P1C with near-incompressibility treatment using the 2x4 B-matrix in 2D (see Section 2.4.3); 1P1C-3INC is 1P1C with near-incompressibility treatment in 3D; 1P2C stands for one point integration with up to second-order correction; 1P2C-INC is 1P2C with near-incompressibility treatment on the second-order correction terms only (designed for higher-order discretizations); and 1P1C-3INC-2C one point integration with near-incompressibility treatment on both the first- and second-order correction terms.

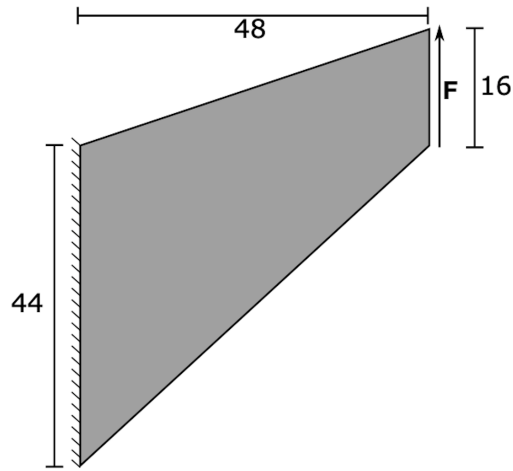## 4.1. 2D Hyperelastic Cook's Membrane Using Linear Quadrilaterals

Figure 1: Cook's membrane problem setup. Problem dimensions is given in mm.

The problem configuration is depicted in Figure 1 with the dimensions given in mm. The membrane is fixed at the left edge and subjected to a uniform vertical dead load at the right edge. The problem parameters are as follows: Poisson ratio $v = 0.4999$; Young's modulus $E = 78.2$ GPa; Traction $F = 100$ N/mm.
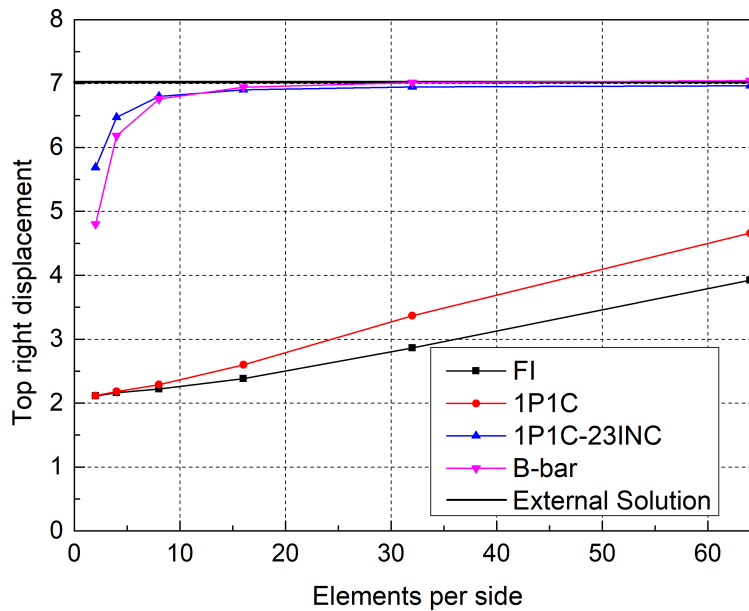

Figure 2: 2D hyperelastic nearly-incompressible Cook's membrane. Top-right-hand-corner displacement versus the number of elements per side. The converged value of the displacement (i.e., "External Solution") is from [38].

We carry out the computations using a sequence of progressively refined meshes and compare a subset of the methods presented here to the classical B-bar approach and a converged reference
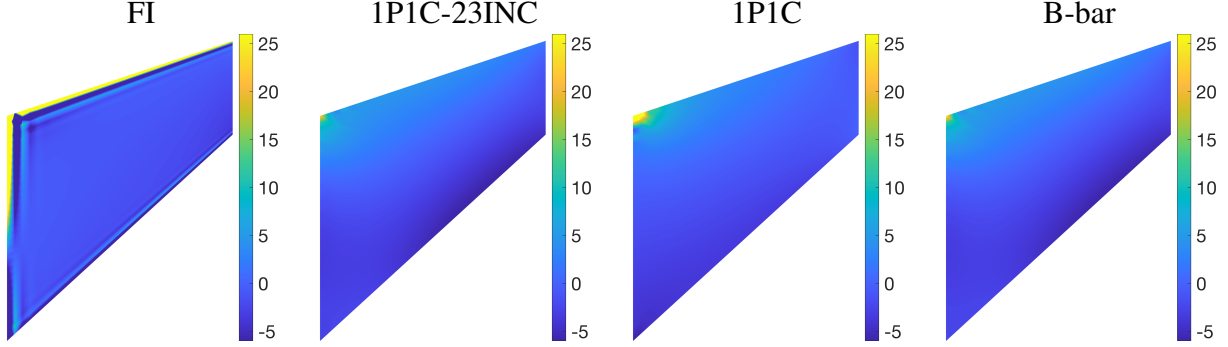
Figure 3: 2D hyperelastic nearly-incompressible Cook's membrane. Contours of the pressure (MPa).

solution from [38]. Figure 2 shows the top-right-hand-corner displacement as a function of the number of elements per side, while Figure 3 shows the pressure distribution on the finest mesh. The problem was computed using a total of 30 load steps in all cases.

The method performance is consistent with the linear-elastic Cook's membrane case shown in [1]. Namely, FI and 1P1C suffer from volumetric locking, which manifests itself in slow convergence of the displacement and oscillations in the pressure contours, while the B-bar and 1P1C-23INC converge to the expected displacement value quickly and produce smooth pressure contours. The 1P1C-23INC formulation appears to be a little softer on the coarse meshes than its B-bar counterpart.

4.2. 2D Plastic Cook's Membrane Using Linear Quadrilaterals

We repeat the computations from the previous section, assuming the material response is now governed by the classical Von Mises isotropic plasticity. We also include both versions of the near-incompressibility treatment (see Section 2.4.3). The problem setup may also be found in [38], with a non-linear hardening law given by

$$\kappa(e_p) = \sigma_0 + (\sigma_\infty - \sigma_0)[1 - \exp(-\delta e_p)] + K e_p, \tag{97}$$

where κ is the radius of the yield surface and e_p is the effective plastic strain. The material parameters are as follows: Shear modulus $\mu = 80.1938$ MPa; Bulk modulus $\kappa = 164.21$ MPa; Initial flow stress $\sigma_0 = 0.450$ MPa; Saturation flow stress $\sigma_\infty = 0.715$ MPa; Saturation exponent $\delta = 16.93$; Linear hardening modulus $K = 0.12924$ MPa. We use 50 load steps to reach the final solution in all cases.

Figures 4 and 5 show the top-right-hand-corner displacement and pressure contours, respectively. As expected, FI and 1P1C exhibit locking, although it is not as severe as in the nearly-incompressible case. 1P1C-23INC and 1P1C-24INC show very similar behavior and alleviate the volumetric locking issue. B-bar, in this case, gives the softest response.
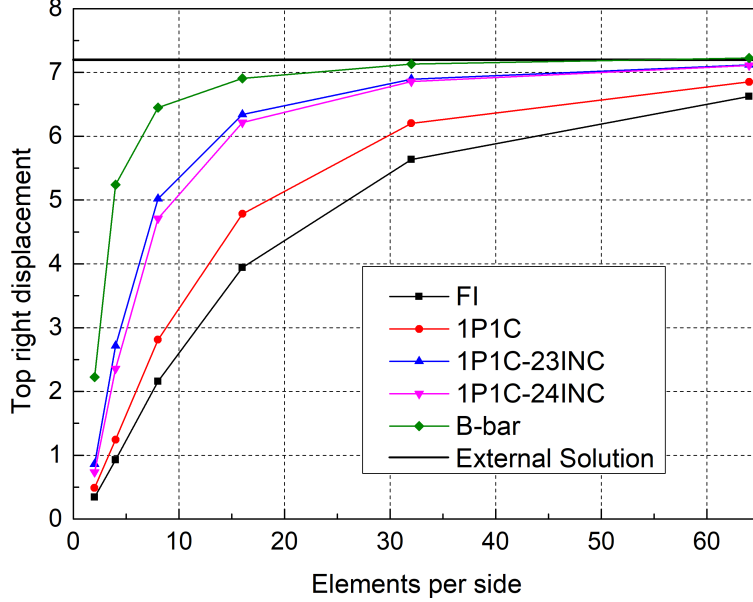
24

Figure 4: 2D plastic Cook's membrane. Top-right-hand-corner displacement versus the number of elements per side. The converged value of the displacement (i.e., "External Solution") is from [38].

4.3. 2D Plastic Taylor Bar Impact Using Linear Quadrilaterals

The Taylor bar impact experiment [55] is widely used as a benchmark validation for the numerical solutions of problems involving large plastic deformations. The problem setup considered here may be found in [56]. The 2D bar has the initial size of 32×6.4 mm. The bar is assigned a downward initial velocity $v = 227$ m/s and the contact is modeled by applying no-penetration and zero tangential stress boundary conditions at the bottom edge. For the plastic material employed, the hardening law is linear and is given by

$$\kappa(e_p) = \sigma_Y + Ke_p. \tag{98}$$

The rest of the problem parameters are as follows: Simulation time $t_\infty = 4 \times 10^{-5}$ s; Poisson ratio $v = 0.3$; Density $\rho = 2700$ kg/m^3; Young's modulus $E = 78.2$ GPa; Yield stress $\sigma_Y = 290$ MPa; Hardening modulus $K = 100$ MPa.

Six meshes (labeled M1-M6), with 5×10, 10×20, 15×30, 20×40, 25×50 and 30×60 elements along the horizontal and vertical direction are employed in the calculations. The number of time steps to complete the analyses were 30 for M1, 60 for M2, 90 for M3, 120 for M4, 150 for M5, and 180 for M6. A comparison is made between FI, 1P1C-23INC, 1P1C-24INC, and B-bar methods. Figure 6 shows the bottom-right-hand-corner displacement. Locking is observed for FI as the spreading of the bottom edge is significantly underpredicted. 1P1C-23INC, 1P1C-24INC, and B-bar all alleviate locking. B-bar converges to a slightly softer response compared to the correction-based methods and the reference result in [56] also plotted in the figure.
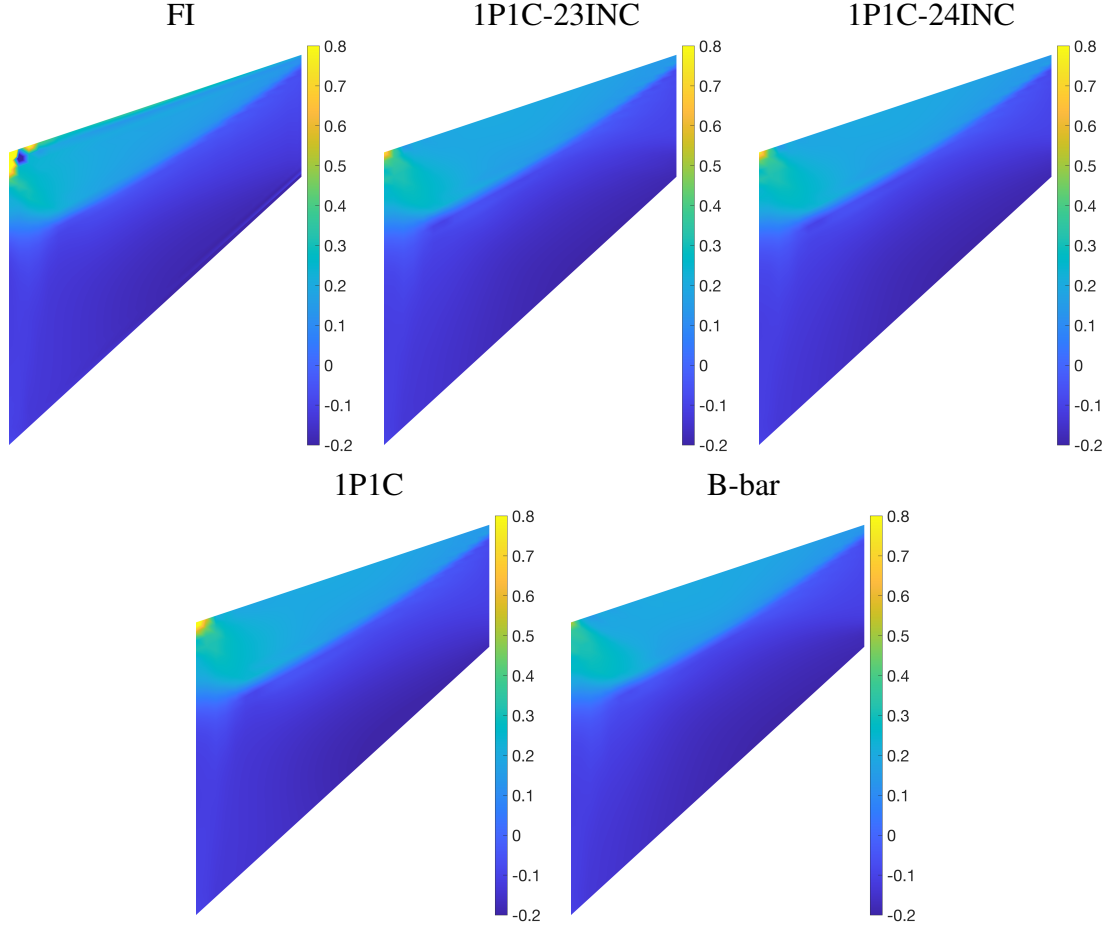
25

Figure 5: 2D plastic Cook's membrane. Contours of the pressure (MPa).

Figure 7 shows the mesh M5 in the final configuration. The locking response of FI is clearly visible. B-bar produces more shearing deformation and overly stretched elements near the center of the bottom edge compared to the correction-based methods. Contours of the vertical component of the Cauchy stress are shown in Figure 8. While no stress oscillations are present in either case, the stress field is visibly different between the B-bar and correction-based methods.

4.4. 3D Plastic Square Taylor Bar Using Linear Hexahedra

We replicate the setup from [57] to simulate the square Taylor bar. We use quarter symmetry, which gives the computational domain of $30 \times 30 \times 60$ mm^3. The remaining problem parameters are as follows: Initial velocity $v = 300$ m/s; Final time $t_\infty = 8 \times 10^{-5}$ s; Poisson ratio $\nu = 0.3$; Density $\rho = 1{,}710$ kg/m^3; Young's modulus $E = 220$ GPa; Yield stress $\sigma_Y = 200$ MPa; Linear hardening modulus $K = 100$ MPa. (Hardening law given by Equation (98) is employed.)

The computations are carried out using the mesh of 2,048 elements. The equivalent plastic strain distribution on the bar deformed configuration is shown in Figure 9. Both FI and 1P1C show
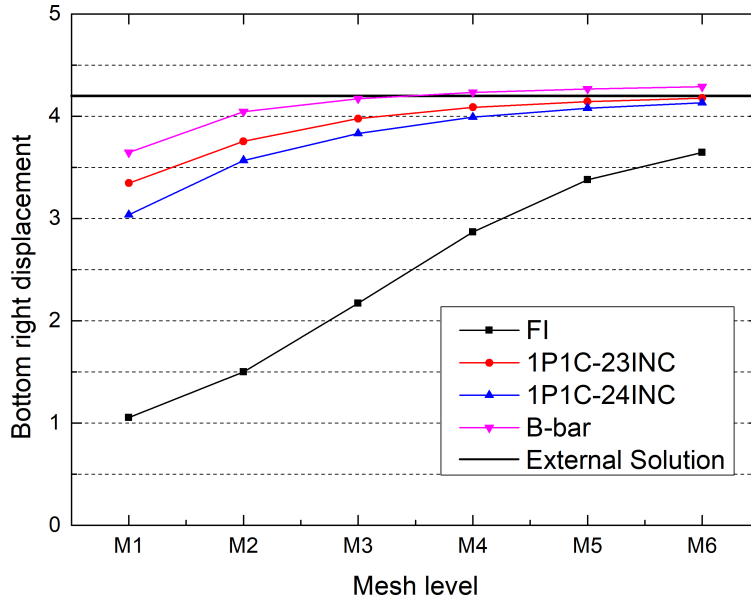
Figure 6: 2D Taylor bar. Bottom-right-hand-corner displacement. The converged value of the displacement (i.e., "External Solution") is from [56].
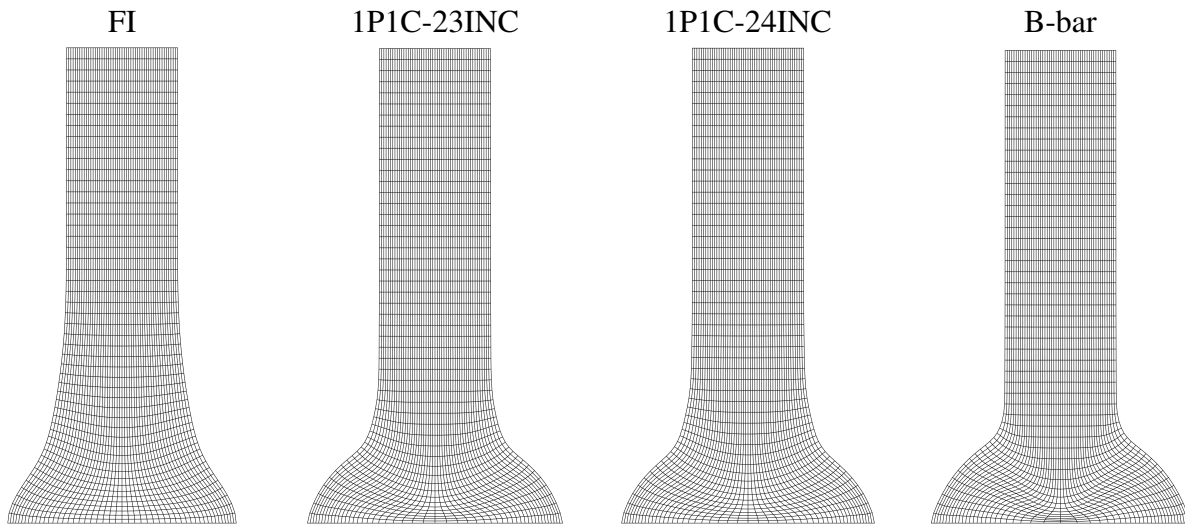

Figure 7: 2D Taylor bar. Mesh M5 in the final configuration.

significant locking, while the correction-based methods give the deformed shape and equivalent plastic strain that are consistent with the results from [57], also shown in the figure. The case from [57] was computed using 2,048 one-point quadrature linear hexes with hourglass control in LS-DYNA, and used an actual contact model between the bar and rigid wall, which results in the mushrooming at the base and some differences in the maximum values of the plastic strain. It is also clear from the figure that, for the present example, including second-order correction terms does not make a significant difference in the results. Although zero-energy modes are possible with the first-order correction for 3D linear hexes (see [1]), they are not triggered in the present
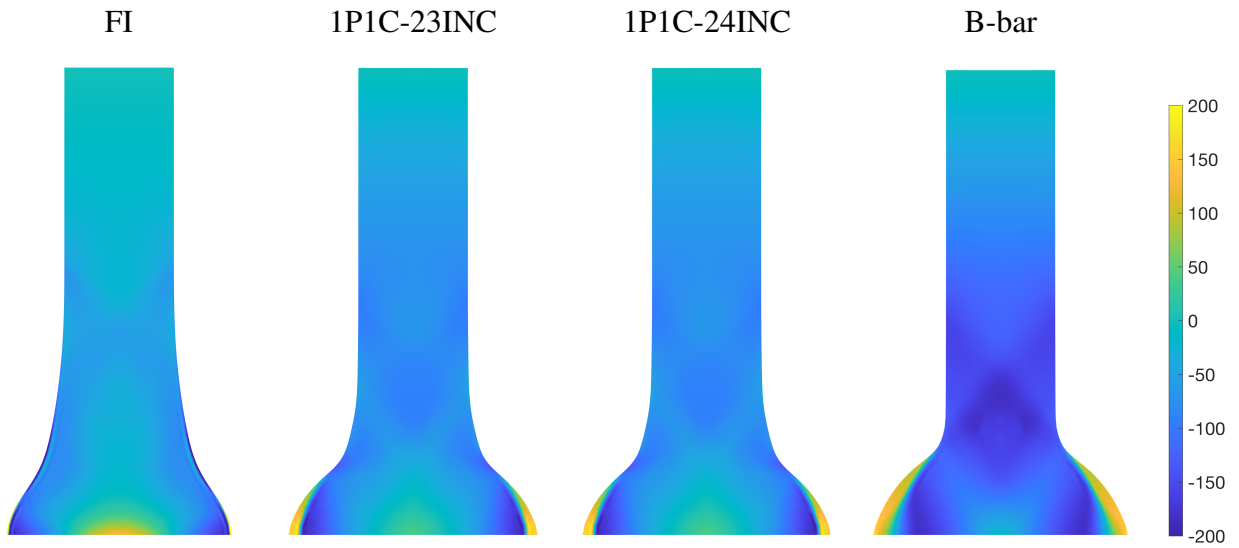
Figure 8: 2D Taylor bar. Contours of the vertical component of the Cauchy stress (σ_{22}) for mesh M5.
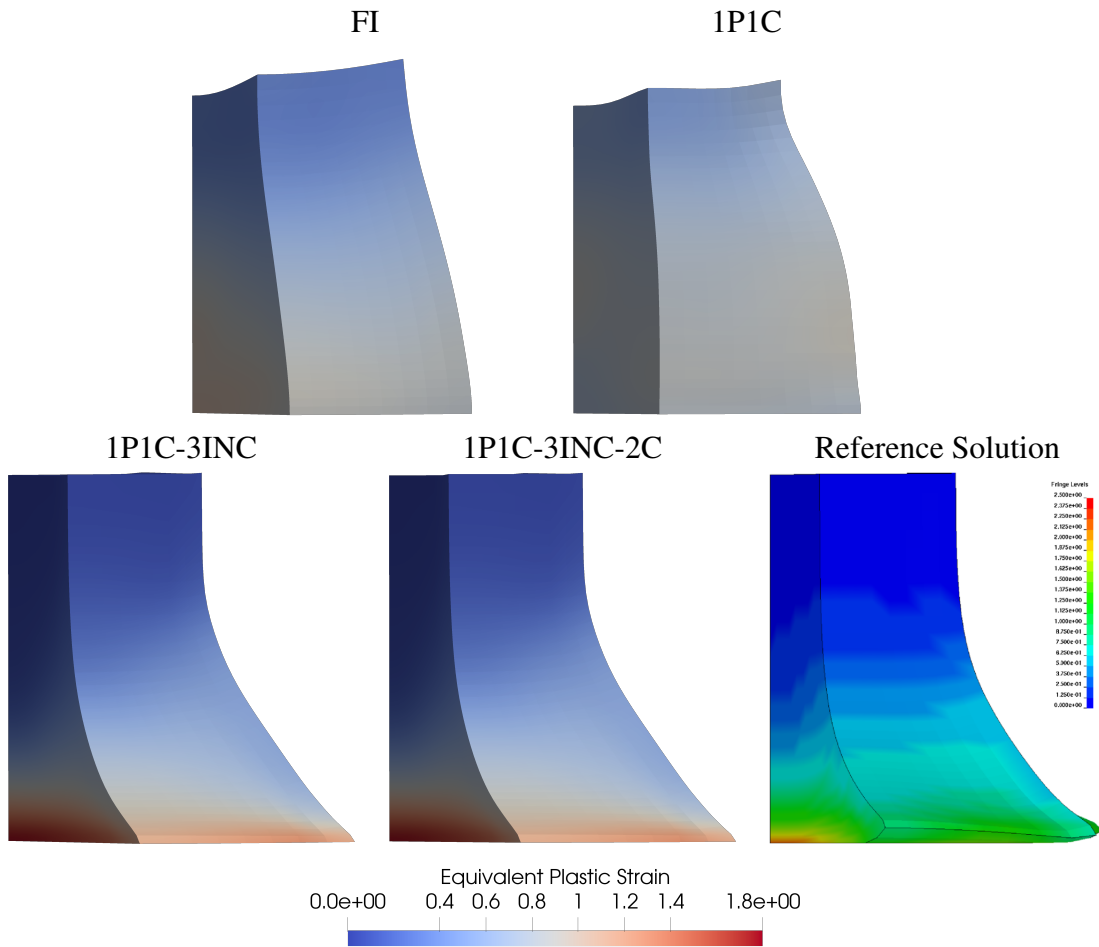

Figure 9: 3D square Taylor bar. Equivalent plastic strain at final time. External solution is from [57]

setup.

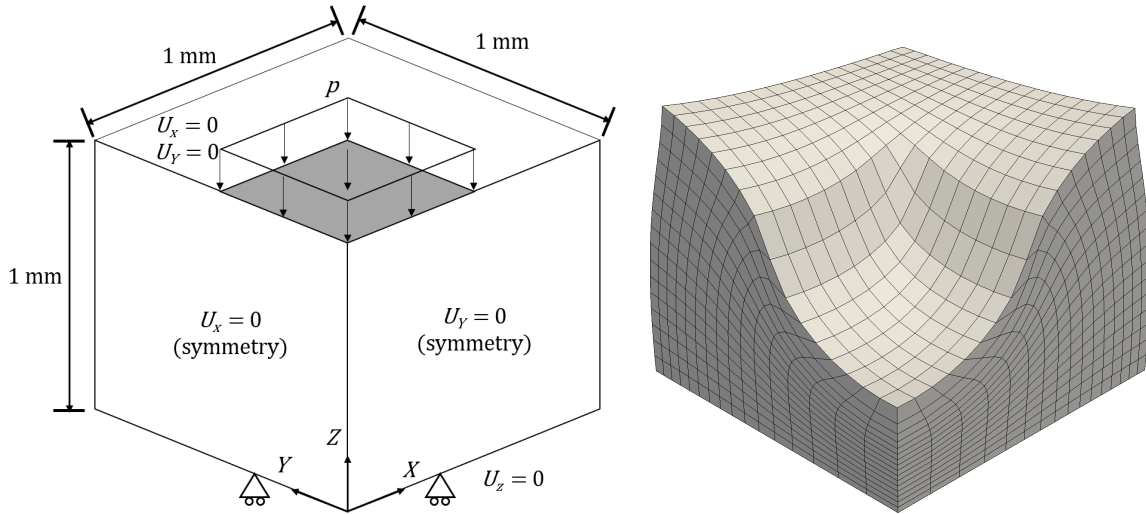## 4.5. 3D Hyperelastic Block Under Compression Using Linear Hexahedra

Figure 10: 3D hyperelastic block under compression. Left: Geometry, boundary conditions, and loading. Right: Deformed configuration and mesh.

This example, studied in [38, 58], is a popular volumetric locking benchmark problem. The geometry, loading and boundary conditions are shown in Figure 10. A downward pressure p is applied as a dead load over the grey area on the top of the block. The bottom plane is constrained in the vertical direction, and the top plane is constrained in horizontal directions. The problem parameters are as follows: Bulk modulus $\kappa = 400{,}889.806$ MPa; Shear modulus $\mu = 80.194$ MPa; Reference compression pressure $p_0 = 4$ MPa, with the loading factors going from from $p/p_0 = 20$ to $p/p_0 = 80$. Quarter symmetry is applied to reduce the computational costs.

The deformed configuration for the 1P1C-3INC computation using the finest mesh and highest load level is shown in Figure 10. The results are consistent with those reported in [58]. Figure 11 shows the results of the mesh refinement study for each load case. Vertical displacement of the central node on the upper surface is the quantity of interest. The displacement is normalized by the height of the block and expressed in percent values. The FI case, as expected, produced severe locking, while the 1P1C-3INC formulation gave rapid convergence to the expected value of the displacement for each load level. We also carried out the computations using the second-order correction, i.e., 1P1C-3INC-2C, but little difference was observed compared to the first-order correction. This observation is consistent with the results reported in Section 4.4.

4.6. 3D Twisted Hyperelastic Beam Using Linear Hexahedra and Quadratic NURBS

This example was introduced in [59] to assess the accuracy and robustness of IGA under high mesh distortion. The geometry, loading, boundary conditions and the von Mises stress plotted on
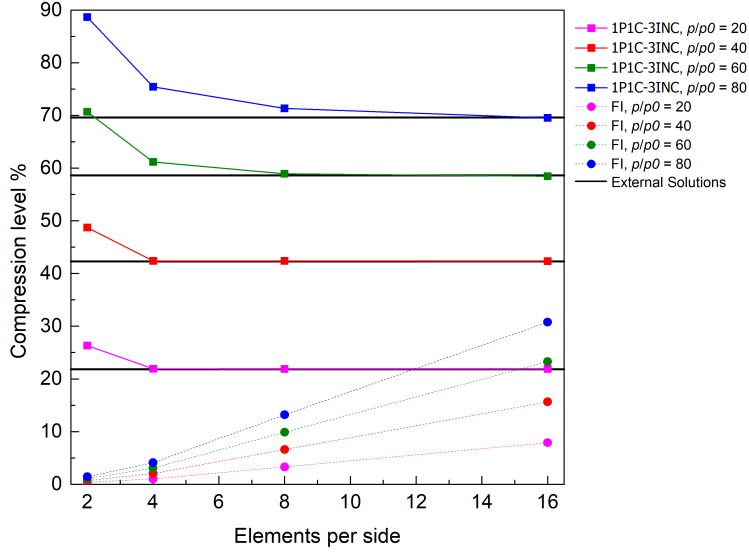
Figure 11: 3D hyperelastic block under compression. Convergence of the vertical displacement of the central node on the upper surface of the block for different levels of the compressive load $p/p_0 = 20, 40, 60, 80$. The displacement is normalized by the height of the block and expressed in percent values. "External Solutions" are the converged values of the displacement from [38].

the deformed near-final configuration are shown in Figure 12. The bottom surface of the beam is fixed in all directions while the top surface is fixed in the vertical direction and has an applied in-plane rotation. We use the same nearly-incompressible hyperelastic material model as the previous example in Section 4.5.

We are interested in the maximum sustainable rotation angle θ and consider three discretizations: 6×6×18 linear hexahedra with 1P1C-3INC, 7×7×19 quadratic NURBS with 1P2C-INC and $7 \times 7 \times 19$ quadratic NURBS with 1P1C-3INC-2C. The deformed configurations corresponding to the three discretizations are shown in Figure 13. The results indicate that C^0 linear hexes with near-incompressibility treatment exhibit no locking and are able to reach 480° of twist; C^1 quadratic NURBS with the 1P2C-INC formulation (i.e., near-incompressibility treatment only on the second-order correction terms) lock fairly early in the computations and are not able to go beyond 126° of twist; C^1 quadratic NURBS with the 1P1C-3INC-2C formulation (i.e., near-incompressibility treatment on the first- and second-order correction terms) exhibit the most robust behavior and reach 492° of twist.

Note that we are able to reach nearly 500° of twist, which is somewhat lower than the maximum sustainable rotation reported in [59]. The discrepancy is attributable to the use of a simple Newton–Raphson technique for nonlinear equation solving in the present work. More advanced nonlinear solution strategies were employed in the original reference to push the computations further.
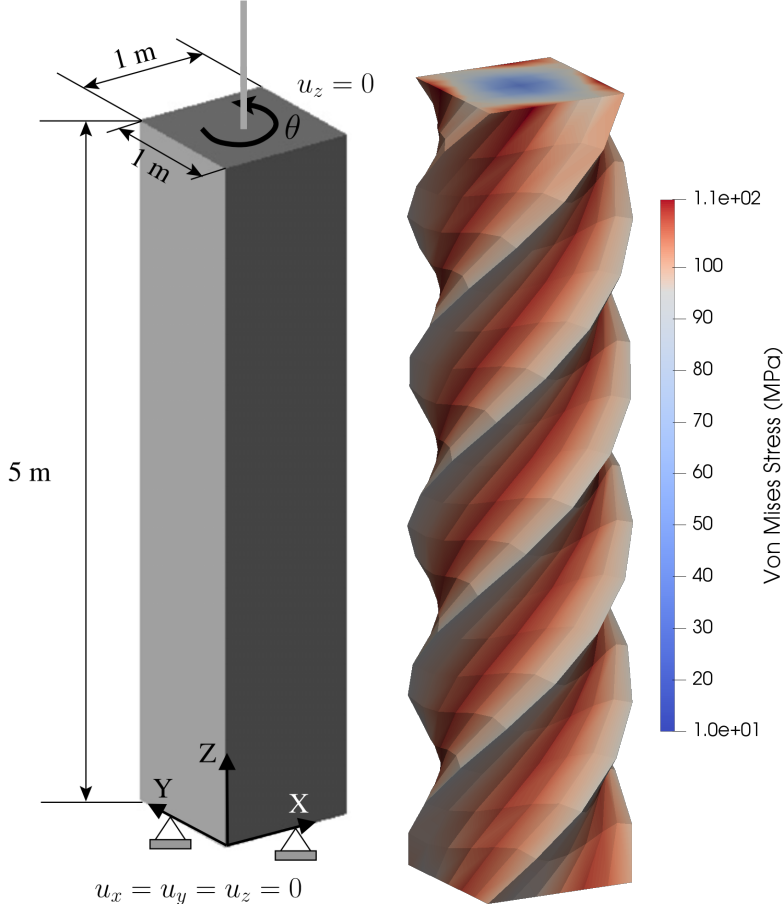
Figure 12: 3D twisted beam. Left: Geometry, boundary conditions, and loading. Right: Near-final configuration ($\theta = 450°$) with the von Mises stress computed using C^1-continuous quadratic NURBS.

4.7. 3D Cylindrical Plastic Taylor Bar Using Quadratic NURBS

We reproduce the setup from [56]. The modeling parameters are as follows: Initial height 23.46 mm; Initial radius 3.91 mm; Initial impact velocity $v = 373$ m/s; Final time $t_\infty = 4 \times 10^{-5}$ s; Poisson ratio $v = 0.3$; Density $\rho = 2700$ kg/m^3; Young's modulus $E = 78.2$ GPa; Yield stress $\sigma_Y = 0.29$ GPa; The hardening rule is given by

$$\kappa(e_p) = \sigma_Y(1 + 0.125e_p)^{0.1}. \tag{99}$$

The problem is computed assuming quarter symmetry and using the meshes of 324, 768, and 1,500 C^1-continuous quadratic NURBS elements.

The deformed shape and distribution of the equivalent plastic strain at the end of the computation are shown in Figures 14 and 15 using the finest mesh. The correction-based methods show better correlation with the experimentally obtained final shape from [60] than the slightly locking FI case. Note that, compared to the results from a similar test case presented in the previous

31

1P1C-3INC on C^0 1P2C-INC on C^1 1P1C-3INC-2C on C^1

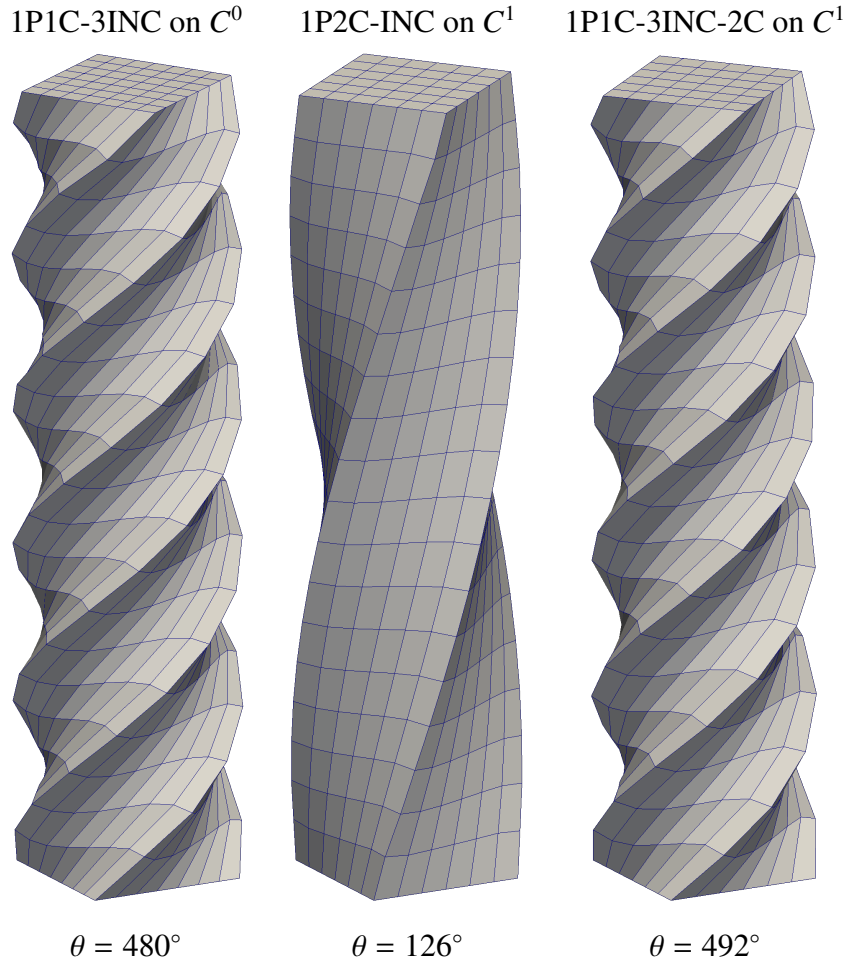$\theta = 480°$ $\theta = 126°$ $\theta = 492°$

Figure 13: 3D twisted beam. Maximum sustainable rotation angle.

section, higher-order NURBS show a lot less volumetric locking under full quadrature than linear hexes, which makes them less reliant on hourglass-control-, B-bar- or correction-type techniques.

Table 1: 3D cylindrical Taylor bar. Summary of results.

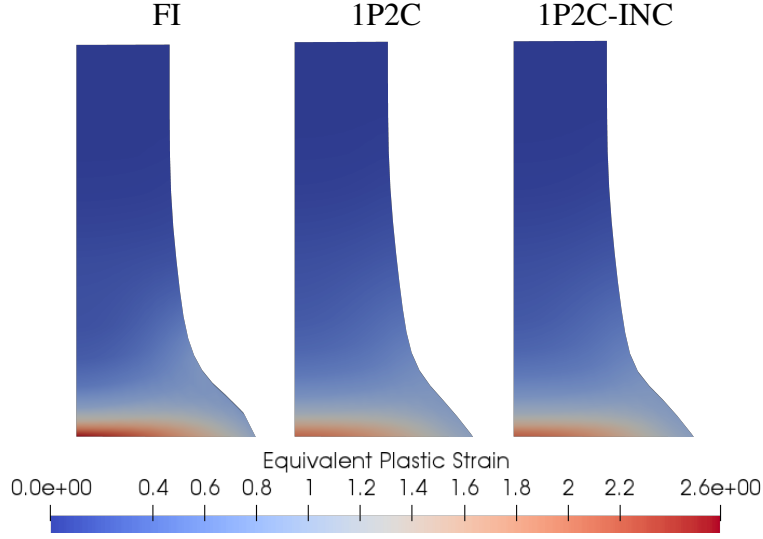| Type	Elements	Bottom Radius (mm)	Height (mm)	Normalized CPU Time
FI	324	7.17587	16.3469	1.0000
FI	768	7.38461	16.4063	3.2083
FI	1500	7.50073	16.4376	7.6903
1P2C	324	7.30374	16.6029	0.3292
1P2C	768	7.35342	16.5867	1.0787
1P2C	1500	7.47174	16.5843	2.5759
1P2C-INC	324	7.62881	16.6929	0.4436
1P2C-INC	768	7.57723	16.6233	1.4776
1P2C-INC	1500	7.54907	16.5959	3.4492
Experiment	-	-	16.51	-

32

Figure 14: 3D cylindrical Taylor bar. Equivalent plastic strain distribution in the domain interior at the end of the computation.
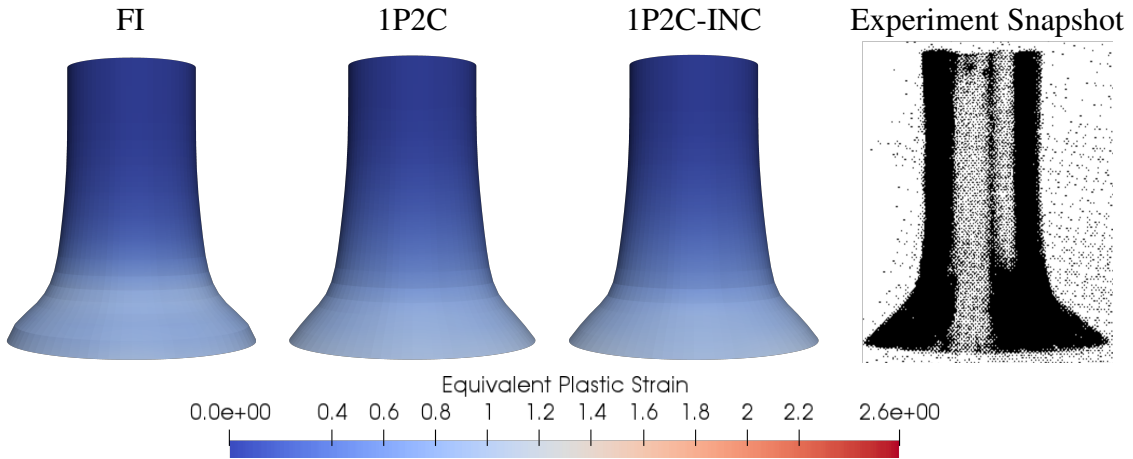

Figure 15: 3D cylindrical Taylor bar. Deformed shape comparison. The experimental snapshot is from [60]

The summary of the bar final-configuration bottom radius and height as well as the normalized CPU time for each run are reported in Table 1. The CPU time calculation includes quadrature and formation of the left-hand-side matrix and right-hand-side vector. The near-incompressibility treatment shows convergence from the softer side for the bottom radius, which is consistent with the observations in [1]. Using the correction-based approaches results in about 60% computational cost savings for the overall CPU time relative to FI. This is quite significant because near-incompressibility treatment, which typically incurs additional computational costs relative to FI, is included at essentially no additional cost in the correction-based formulations.

4.8. 3D Uniaxial Compression of a Concrete Prism Using the M7 Microplane Model

The setup is from [61], where the experimental compression tests on concrete prisms were conducted. A 50×100×100 mm concrete prism with a square cross section is subjected to a downward displacement-controlled loading, with a maximum global compressive strain 0.01. The M7 model parameters are taken from [39]. Using the notation of the aforementioned reference, they are as follows: Young's modulus $E = 30{,}173$ MPa; $k_1 = 1 \times 10^{-4}$; $k_2 = 110$; $k_3 = 20$; $k_4 = 40$; $k_5 = 1 \times 10^{-4}$; Poisson ratio $v = 0.18$. Following the procedure in [43], a 1% random perturbation to the parameter k_1 is generated to prevent many elements entering the softening regime at the same time. An adaptive time stepping technique is used to help convergence due to the nonlinear, strain-softening nature of the M7 concrete model. We carry out implicit analysis using three meshes (denoted by M1, M2 and M3) comprised of 512, 1,000 and 1,728 linear hexahedral elements, respectively.
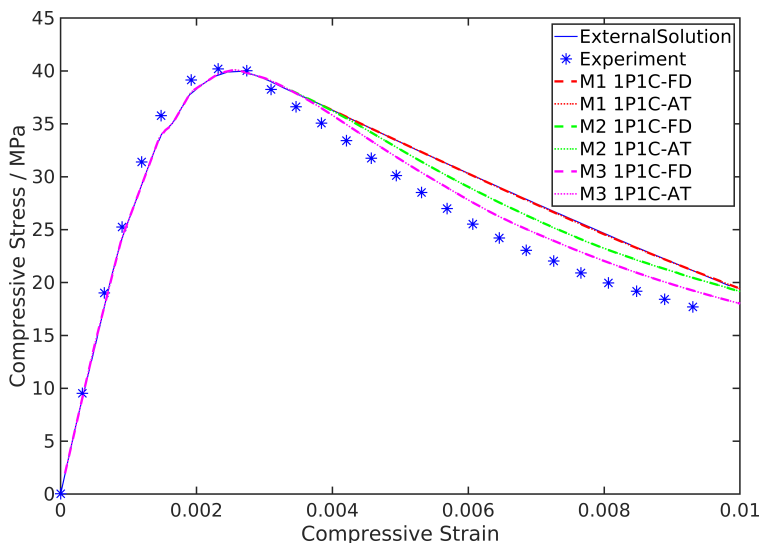

Figure 16: Compression of a concrete prism. Global axial stress-strain response. Suffix "FD" denotes finite-difference approximation of the tangent stiffness, while suffix "AT" denotes the analytical tangent stiffness. External solution is from [39] and experimental result is from [61].

Figure 16 shows the global stress-strain response and an excellent agreement between the experimental data of [61], computational results of [39], and and our correction-based approach. Only the first-order correction is employed in this case. Comparison of the analytical and finite-difference-based formulation for the tangent stiffness is also presented and reveals virtually no difference in the global stress-strain response predictions. We note that the agreement between the experimental data and correction-based methods improves in the postpeak response as the mesh is refined.

Table 2 provides a CPU time comparison between the FI and correction-based methods for M2. The latter include the analytical expressions vs. the finite-difference approximation of the tangent stiffness. (The FI case used the analytical tangent.) Note that, as before, the CPU time computation

Table 2: Compression of a concrete prism. Number of time steps and normalized CPU time for M2.

Formulation	Total Number of Time Steps	Normalized CPU Time
1P1C-FD	1,378	0.4502
1P1C-AT	1,819	0.3193
FI-AT	2,040	1.0000

includes all aspects of the analysis exclude equation solving (time stepping, quadrature and matrix assembly). We also include a number of adaptive time steps used to complete the simulation. Note that the full quadrature case required over 2,000 steps to complete the calculations, while the correction-based finite-difference approach used under 1,400 steps. The correction-based formulation with the analytical tangent gave the best CPU time performance, while the correction-based formulation using the finite-difference tangent came in second. The additional costs associated with the finite-difference-based evaluation of the tangent stiffness do not seem significant, which makes this a practical methodology for use with complex constitutive material models.
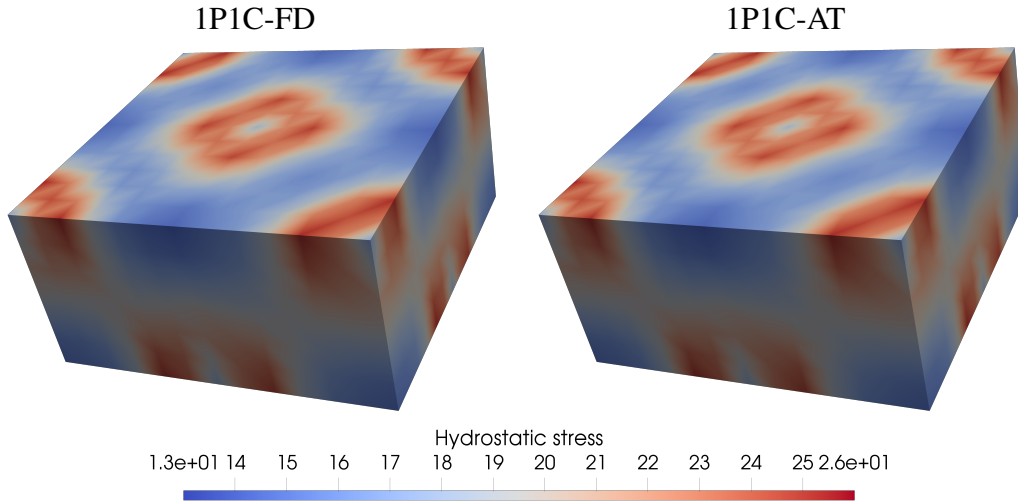

Figure 17: Compression of a concrete prism. Hydrostatic stress (MPa) at final time.

The hydrostatic stress contours at final time are plotted in Figure 17, showing little-to-no difference between the analytical and finite-difference material tangent definitions.

5. Conclusion

In this work, one-point integration and Taylor series expansion techniques developed in [1] for linear elasticity are reformulated for the fully nonlinear case. The updated Lagrangian formulation in combination with the rate form of the constitutive laws is felt to be a particularly suitable framework for the application of the Taylor-expansion-based methods. The evolution equations for the Cauchy stress parametric gradients are derived in a straightforward fashion. The increment

of the stress parametric gradient (first and second) appears to be well approximated using a product of the material tangent stiffness and the increment of the strain parametric gradient (first and second). The framework respects objectivity and accommodates many constitutive laws, which makes it well suited for large-deformation analysis. The resulting formulation is more straightforward to develop and implement than the methods based on the total Lagrangian approach. It is also free from user-defined parameters. The treatment of near-incompressibility is straightforward, computationally efficient, and robust.

The effectiveness of the methods developed is demonstrated on a set of numerical examples using both linear FEM and quadratic NURBS discretizations. Several constitutive models with varying levels of complexity are employed in the examples showing the versatility of the proposed approach. The examples show applications ranging from highly dynamic impact of metal specimens to quasi-static concrete failure. Good agreement with the experimental results is obtained in all cases where the experimental date were available. It is important to note that the finite-difference approximation of the material tangent stiffness used to compute the stress gradient increments appears to give stable and accurate results for a complex concrete failure model without introducing significant additional computational costs. This opens the possibility to effectively use the proposed methodology for problems where the material tangent stiffness is not readily available.

Acknowledgments

References

[1] G. Moutsanidis, W. Li, and Y. Bazilevs. Reduced quadrature for FEM, IGA and meshfree methods. *Computer Methods in Applied Mechanics and Engineering*, 373:113521, 2021.

[2] J.-S. Chen, M. Hillman, and S.-W. Chi. Meshfree methods: progress made after 20 years. *Journal of Engineering Mechanics*, 143(4):04017001, 2017.

[3] T. J. Hughes, J. A. Cottrell, and Y. Bazilevs. Isogeometric analysis: CAD, finite elements, NURBS, exact geometry and mesh refinement. *Computer Methods in Applied Mechanics and Engineering*, 194(39-41):4135–4195, 2005.

[4] J. A. Cottrell, T. J. Hughes, and Y. Bazilevs. *Isogeometric Analysis: Toward Integration of CAD and FEA*. John Wiley & Sons, 2009.

[5] D. Sulsky, Z. Chen, and H. L. Schreyer. A particle method for history-dependent materials. *Computer Methods in Applied Mechanics and Engineering*, 118(1-2):179–196, 1994.

[6] G. Moutsanidis, C. C. Long, and Y. Bazilevs. Iga-mpm: The isogeometric material point method. *Computer Methods in Applied Mechanics and Engineering*, 372:113346, 2020.

[7] W. K. Liu, J. S.-J. Ong, and R. A. Uras. Finite element stabilization matrices-a unification approach. *Computer Methods in Applied Mechanics and Engineering*, 53(1):13–46, 1985.

[8] J. Schulz. Finite element hourglassing control. *International Journal for Numerical Methods in Engineering*, 21(6):1039–1048, 1985.

[9] D. Flanagan and T. Belytschko. A uniform strain hexahedron and quadrilateral with orthogonal hourglass control. *International Journal for Numerical Methods in Engineering*, 17(5):679–706, 1981.

[10] T. Belytschko, J. S.-J. Ong, W. K. Liu, and J. M. Kennedy. Hourglass control in linear and nonlinear problems. *Computer Methods in Applied Mechanics and Engineering*, 43(3):251–276, 1984.

[11] S. Reese. On a physically stabilized one point finite element formulation for three-dimensional finite elasto-plasticity. *Computer Methods in Applied Mechanics and Engineering*, 194(45-47):4685–4715, 2005.

[12] W. K. Liu, S. Jun, and Y. F. Zhang. Reproducing kernel particle methods. *International Journal for Numerical Methods in Fluids*, 20(8-9):1081–1106, 1995.

[13] J.-S. Chen, C. Pan, C.-T. Wu, and W. K. Liu. Reproducing kernel particle methods for large deformation analysis of non-linear structures. *Computer Methods in Applied Mechanics and Engineering*, 139(1-4):195–227, 1996.

[14] J.-S. Chen, C.-T. Wu, S. Yoon, and Y. You. A stabilized conforming nodal integration for Galerkin mesh-free methods. *International journal for numerical methods in engineering*, 50(2):435–466, 2001.

[15] S. Beissel and T. Belytschko. Nodal integration of the element-free galerkin method. *Computer methods in applied mechanics and engineering*, 139(1-4):49–74, 1996.

[16] T. Belytschko, Y. Guo, W. Kam Liu, and S. Ping Xiao. A unified stability analysis of meshless particle methods. *International Journal for Numerical Methods in Engineering*, 48(9):1359–1400, 2000.

[17] P. Randles and L. Libersky. Normalized SPH with stress points. *International Journal for Numerical Methods in Engineering*, 48(10):1445–1462, 2000.

[18] C. Dyka, P. Randles, and R. Ingel. Stress points for tension instability in SPH. *International Journal for Numerical Methods in Engineering*, 40(13):2325–2341, 1997.

[19] C. Dyka and R. Ingel. An approach for tension instability in smoothed particle hydrodynamics (SPH). *Computers & structures*, 57(4):573–580, 1995.

[20] J. Chen, W. Hu, M. Puso, Y. Wu, and X. Zhang. Strain smoothing for stabilization and regularization of Galerkin meshfree methods. In *Meshfree methods for partial differential equations III*, pages 57–75. Springer, 2007.

[21] M. Puso, J. Chen, E. Zywicz, and W. Elmer. Meshfree and finite element nodal integration methods. *International Journal for Numerical Methods in Engineering*, 74(3):416–446, 2008.

[22] D. Wang and J.-S. Chen. A Hermite reproducing kernel approximation for thin-plate analysis with sub-domain stabilized conforming integration. *International Journal for Numerical Methods in Engineering*, 74(3):368–390, 2008.

[23] D. Wang and Z. Lin. Dispersion and transient analyses of Hermite reproducing kernel Galerkin meshfree method with sub-domain stabilized conforming integration for thin beam and plate structures. *Computational Mechanics*, 48(1):47–63, 2011.

[24] T. Nagashima. Node-by-node meshless approach and its applications to structural analyses. *International Journal for Numerical Methods in Engineering*, 46(3):341–385, 1999.

[25] G. Liu, G. Zhang, Y. Wang, Z. Zhong, G. Li, and X. Han. A nodal integration technique for meshfree radial point interpolation method (NI-RPIM). *International Journal of Solids and Structures*, 44(11-12):3840–3860, 2007.

[26] S. Li and W. K. Liu. Reproducing kernel hierarchical partition of unity, part I—formulation and theory. *International Journal for Numerical Methods in Engineering*, 45(3):251–288, 1999.

[27] J.-S. Chen, X. Zhang, and T. Belytschko. An implicit gradient model by a reproducing kernel strain regularization in strain localization problems. *Computer methods in applied mechanics and engineering*, 193(27-29):2827–2844, 2004.

[28] M. Hillman and J.-S. Chen. An accelerated, convergent, and stable nodal integration in galerkin meshfree methods for linear and nonlinear mechanics. *International Journal for Numerical Methods in Engineering*, 107(7):603–630, 2016.

[29] J. Bonet and S. Kulasegaram. Correction and stabilization of smooth particle hydrodynamics methods with applications in metal forming simulations. *International journal for numerical methods in engineering*, 47(6):1189–1214, 2000.

[30] Q. Duan and T. Belytschko. Gradient and dilatational stabilizations for stress-point integration in the element-free Galerkin method. *International Journal for Numerical Methods in Engineering*, 77(6):776–798, 2009.

[31] T. J. Hughes, A. Reali, and G. Sangalli. Efficient quadrature for nurbs-based isogeometric analysis. *Computer Methods in Applied Mechanics and Engineering*, 199(5-8):301–313, 2010.

[32] R. R. Hiemstra, F. Calabro, D. Schillinger, and T. J. Hughes. Optimal and reduced quadrature rules for tensor product and hierarchically refined splines in isogeometric analysis. *Computer Methods in Applied Mechanics and Engineering*, 316:966–1004, 2017.

[33] Z. Zou, T. Hughes, M. Scott, R. Sauer, and E. Savitha. Galerkin formulations of isogeometric shell analysis: Alleviating locking with greville quadratures and higher-order elements. *Computer Methods in Applied Mechanics and Engineering*, 380:113757, 2021.

[34] Z. Zou, T. Hughes, M. Scott, D. Miao, and R. Sauer. Efficient and robust quadratures for isogeometric analysis: Reduced gauss and gauss–greville rules. *Computer Methods in Applied Mechanics and Engineering*, 392:114722, 2022.

[35] T. Belytschko, W. K. Liu, B. Moran, and K. Elkhodary. *Nonlinear Finite Elements for Continua and Structures*. John wiley & sons, 2014.

[36] Y. Bazilevs, D. Kamensky, G. Moutsanidis, and S. Shende. Residual-based shock capturing in solids. *Computer Methods in Applied Mechanics and Engineering*, 358:112638, 2020.

[37] T. J. Hughes. Generalization of selective integration procedures to anisotropic and nonlinear media. *International Journal for Numerical Methods in Engineering*, 15(9):1413–1418, 1980.

[38] T. Elguedj, Y. Bazilevs, V. M. Calo, and T. J. Hughes. B and f projection methods for nearly incompressible linear and non-linear elasticity and plasticity using higher-order NURBS elements. *Computer Methods in Applied Mechanics and Engineering*, 197(33-40):2732–2762, 2008.

[39] F. C. Caner and Z. P. Bažant. Microplane model M7 for plain concrete. I: Formulation. *Journal of Engineering Mechanics*, 139(12):1714–1723, 2013.

[40] M. E. Gurtin, E. Fried, and L. Anand. *The Mechanics and Thermodynamics of Continua*. Cambridge University Press, 2010.

[41] T. J. Hughes. *The Finite Element Method: Linear Static and Dynamic Finite Element Analysis*. Courier Corporation, 2012.

[42] D. S. Malkus and T. J. Hughes. Mixed finite element methods—reduced and selective integration techniques: a unification of concepts. *Computer Methods in Applied Mechanics and Engineering*, 15(1):63–81, 1978.

[43] H. T. Nguyen, F. C. Caner, and Z. P. Bažant. Conversion of explicit microplane model with boundaries to a constitutive subroutine for implicit finite element programs. *International Journal for Numerical Methods in Engineering*, 122(6):1563–1577, 2021.

[44] J. C. Simo and T. J. Hughes. *Computational Inelasticity*, volume 7. Springer Science & Business Media, 2006.

[45] J. C. Simo and R. L. Taylor. Consistent tangent operators for rate-independent elastoplasticity. *Computer Methods in Applied Mechanics and Engineering*, 48(1):101–118, 1985.

[46] C. Miehe. Numerical computation of algorithmic (consistent) tangent moduli in large-strain computational inelasticity. *Computer Methods in Applied Mechanics and Engineering*, 134(3-4):223–240, 1996.

[47] Z. P. Bažant and B. H. Oh. Microplane model for fracture analysis of concrete structures. Technical report, Northwestern Univ Evanston Il Technological Inst, 1983.

[48] Z. P. Bažant and B. H. Oh. Microplane model for progressive fracture of concrete and rock. *Journal of Engineering Mechanics*, 111(4):559–582, 1985.

[49] Z. P. Bažant and P. C. Prat. Microplane model for brittle-plastic material: I. Theory. *Journal of Engineering Mechanics*, 114(10):1672–1688, 1988.

[50] Z. P. Bažant, Y. Xiang, and P. C. Prat. Microplane model for concrete. I: Stress-strain boundaries and finite strain. *Journal of Engineering Mechanics*, 122(3):245–254, 1996.

[51] Z. P. Bažant, F. C. Caner, I. Carol, M. D. Adley, and S. A. Akers. Microplane model M4 for concrete. I: Formulation with work-conjugate deviatoric stress. *Journal of Engineering Mechanics*, 126(9):944–953, 2000.

[52] Z. P. Bažant and F. C. Caner. Microplane model M5 with kinematic and static constraints for concrete fracture and anelasticity. I: Theory. *Journal of Engineering Mechanics*, 131(1):31–40, 2005.

[53] F. C. Caner and Z. P. Bažant. Microplane model M6F for fiber reinforced concrete. In *COMPLAS XI: proceedings of the XI International Conference on Computational Plasticity: fundamentals and applications*, pages 796–807. CIMNE, 2011.

[54] Z. P. Bažant and B. H. Oh. Efficient numerical integration on the surface of a sphere. *ZAMM-Journal of Applied Mathematics and Mechanics/Zeitschrift für Angewandte Mathematik und Mechanik*, 66(1):37–49, 1986.

[55] G. I. Taylor. The use of flat-ended projectiles for determining dynamic yield stress I. Theoretical considerations. *Proceedings of the Royal Society of London. Series A. Mathematical and Physical Sciences*, 194(1038):289–299, 1948.

[56] G. Moutsanidis, J. J. Koester, M. R. Tupek, J.-S. Chen, and Y. Bazilevs. Treatment of near-incompressibility in meshfree and immersed-particle methods. *Computational Particle Mechanics*, 7(2):309–327, 2020.

[57] D. J. Benson, Y. Bazilevs, E. De Luycker, M.-C. Hsu, M. Scott, T. Hughes, and T. Belytschko. A generalized finite element formulation for arbitrary basis functions: from isogeometric analysis to XFEM. *International Journal for Numerical Methods in Engineering*, 83(6):765–785, 2010.

[58] S. Reese, P. Wriggers, and B. Reddy. A new locking-free brick element technique for large deformation problems in elasticity. *Computers & Structures*, 75(3):291–304, 2000.

[59] S. Lipton, J. A. Evans, Y. Bazilevs, T. Elguedj, and T. J. Hughes. Robustness of isogeometric structural discretizations under severe mesh distortion. *Computer Methods in Applied Mechanics and Engineering*, 199(5-8):357–373, 2010.

[60] M. L. Wilkins and M. W. Guinan. Impact of cylinders on a rigid boundary. *Journal of Applied Physics*, 44(3):1200–1206, 1973.

[61] J. G. van Mier. Multiaxial strain-softening of concrete. *Materials and Structures*, 19(3):190–200, 1986.

[62] L. Dalcin, N. Collier, P. Vignal, A. Côrtes, and V. M. Calo. Petiga: A framework for high-performance isogeometric analysis. *Computer Methods in Applied Mechanics and Engineering*, 308:151–181, 2016.